

**Measurement of photons via conversion pairs
with the PHENIX experiment at RHIC**

A Thesis Presented

by

Torsten Dahms

to

The Graduate School

in Partial Fulfillment of the Requirements

for the Degree of

Master of Arts

in

Physics

Stony Brook University

May 2005

Stony Brook University

The Graduate School

Torsten Dahms

We, the Thesis committee for the above candidate for the Master of Arts degree, hereby recommend acceptance of the Thesis.

Axel Drees, Thesis Advisor

Professor, Department of Physics and Astronomy, Stony Brook University

Edward Shuryak

Professor, Department of Physics and Astronomy, Stony Brook University

Michael M. Rijssenbeek

Professor, Department of Physics and Astronomy, Stony Brook University

This Thesis is accepted by the Graduate School.

Dean of the Graduate School

Abstract of the Thesis

**Measurement of photons via conversion pairs
with the PHENIX experiment at RHIC**

by

Torsten Dahms

Master of Arts

in

Physics

Stony Brook University

2005

Thermal photons detected by PHENIX can provide information about the temperature of a possible QGP produced at RHIC. We present a new method identifying photons by measuring e^+e^- -pairs from photon conversions in the beam pipe.

These conversions are reconstructed in PHENIX under the assumption that the tracks originate from the collision vertex. This effectively leads to a misreconstruction of the electron momenta. As a result the conversion pairs acquire an apparent mass and a characteristic orientation relative to the magnetic field

direction. These properties can be used to distinguish conversion pairs from Dalitz decays.

We demonstrate the feasibility of this method and show a photon p_T spectrum in the region of 0.8–2.4 GeV/c from Au + Au collisions at $\sqrt{s_{NN}} = 62.4$ GeV.

To my family

Contents

	List of Figures	viii
	Acknowledgements	xii
1	Introduction	1
1.1	Quark Gluon Plasma and RHIC	1
1.2	Thermal Photons	4
2	The PHENIX Experiment	8
2.1	Global Detectors	10
2.2	The Central Arm	13
2.2.1	The Central Arm Magnet	13
2.2.2	The Drift Chambers	15
2.2.3	The Pad Chambers	18
2.2.4	The RICH	20
2.2.5	The Electromagnetic Calorimeters	21

3	Analysis	23
3.1	Dataset and Run Selection	23
3.2	Electron Identification	24
3.3	Monte Carlo Simulations	27
3.4	e^+e^- -pairs	31
3.4.1	Photon Conversions in PHENIX	33
3.4.2	Pair Cuts	38
3.4.3	Peak Extraction	42
3.5	Correction of modified MC Simulation	50
3.6	Correction for Acceptance and Efficiency	51
3.7	Cocktail Comparison	57
4	Systematic Errors	62
4.1	Electron ID and Conversion Cuts	62
4.2	The Cocktail	66
5	Result and Summary	67
	Bibliography	70
A	Run List	75

List of Figures

1.1	Energy density in QCD	2
1.2	Phase diagram	3
1.3	Theoretical predictions of thermal photons RHIC	5
1.4	Measurement of direct photons at WA98	6
1.5	Measurement of direct photons at PHENIX	6
2.1	PHENIX Detector	11
2.2	BBC	12
2.3	Central Magnets in “++” configuration	14
2.4	DC frame	16
2.5	DC wire layout	17
2.6	DC momentum reconstruction	18
2.7	PC design	20
2.8	RICH	21
2.9	PbSc Calorimeter	22

3.1	π^0 p_T reference spectrum	28
3.2	Comparison of the active area	30
3.3	Raw invariant mass spectrum of e^+e^- -pairs	33
3.4	DC track reconstruction	35
3.5	Constellations of e^+e^- -pairs in the PHENIX detector	37
3.6	e^+e^- -pair p_T spectrum	37
3.7	Azimuthal opening angle of simulated e^+e^- -pairs	40
3.8	Azimuthal opening angle of real e^+e^- -pairs	41
3.9	Schematic of the pair orientation in the magnetic field	42
3.10	Orientation of simulated e^+e^- -pairs in the magnetic field	43
3.11	Orientation of real e^+e^- -pairs in the magnetic field	43
3.12	Invariant mass spectrum after applying pair cuts	45
3.13	Subtracted e^+e^- -pair mass spectrum in the east arm (I/II)	46
3.14	Subtracted e^+e^- -pair mass spectrum in the east arm (II/II)	47
3.15	Subtracted e^+e^- -pair mass spectrum in the west arm (I/II)	48
3.16	Subtracted e^+e^- -pair mass spectrum in the west arm (II/II)	49
3.17	Raw photon p_T spectrum	50
3.18	Comparison of modified and generic MC simulation in the east arm	52

3.19	Comparison of modified and generic MC simulation in the west arm	52
3.20	Ratio of modified and generic MC simulation in the east arm .	53
3.21	Ratio of modified and generic MC simulation in the west arm	53
3.22	Correction function for acceptance and reconstruction efficiency in the east arm	55
3.23	Correction function for acceptance and reconstruction efficiency in the west arm	55
3.24	Corrected photon p_T spectrum	56
3.25	Comparison of corrected photon p_T spectrum with cocktail for east arm	58
3.26	Comparison of corrected photon p_T spectrum with cocktail for east arm (zoom)	59
3.27	Comparison of corrected photon p_T spectrum with cocktail for west arm	60
3.28	Comparison of corrected photon p_T spectrum with cocktail for west arm (zoom)	61
4.1	Systematic uncertainty of cuts for e^+e^- -pairs in the east arm (I/II)	64

4.2	Systematic uncertainty of cuts for e^+e^- -pairs in the east arm (II/II)	64
4.3	Systematic uncertainty of cuts for e^+e^- -pairs in the west arm (I/II)	65
4.4	Systematic uncertainty of cuts for e^+e^- -pairs in the west arm (II/II)	65
5.1	Photon p_T spectrum	68
5.2	Ratio of measured photon p_T spectrum and cocktail	68

Acknowledgements

First I would like to thank Axel Drees who accompanied me as my advisor. He introduced me to the field of heavy ion physics and gave me the great opportunity to work for him and the Relativistic Heavy Ion Group at Stony Brook. I will be always grateful for his support and confidence in my work.

I highly appreciate the substantial help and cooperation from Ralf Averbek and Sasha Milov. I would like to thank everybody else in the group at Stony Brook, I enjoyed working in such a pleasant atmosphere.

I am indebted to everybody who is involved in the exchange program between the physics department of the University of Würzburg and Stony Brook University for all their efforts to organize my stay here.

I owe my warmest thanks to my family who always encouraged me. Without their love and support this work would not have been possible.

This work was supported by the German Academic Exchange Service (DAAD) and the Research Foundation of State University of New York.

Chapter 1

Introduction

1.1 Quark Gluon Plasma and RHIC

The Relativistic Heavy Ion Collider at the BNL and its four experiments PHENIX, BRAHMS, PHOBOS and STAR were build to search for a new state of matter in Au + Au collisions – the quark-gluon plasma (QGP). According to QCD, quarks are confined to hadrons and exist only in pairs of two or three. They are held together by the exchange particles of the strong interaction, the gluons. The strength of this force depends on the coupling constant α_s which depends on the momentum transfer q^2 :

$$\alpha_s \sim \frac{1}{\ln(q^2/\Lambda^2)} \quad (1.1)$$

For small distances the coupling constant is small and the quarks act as

quasi free particles. This behavior is called asymptotic freedom¹ [1] and a perturbative description is possible. For large distances α_s increases and the quarks will be confined; a non perturbative approach is possible [5].

Calculations for high temperatures propose a phase shift to a state of deconfined quarks and gluons at a critical temperature of $T_c \approx 170$ MeV; this state is called the quark-gluon plasma [6]. The increase of the energy density as predicted in recent lattice QCD calculations [7] is shown in Fig. 1.1.

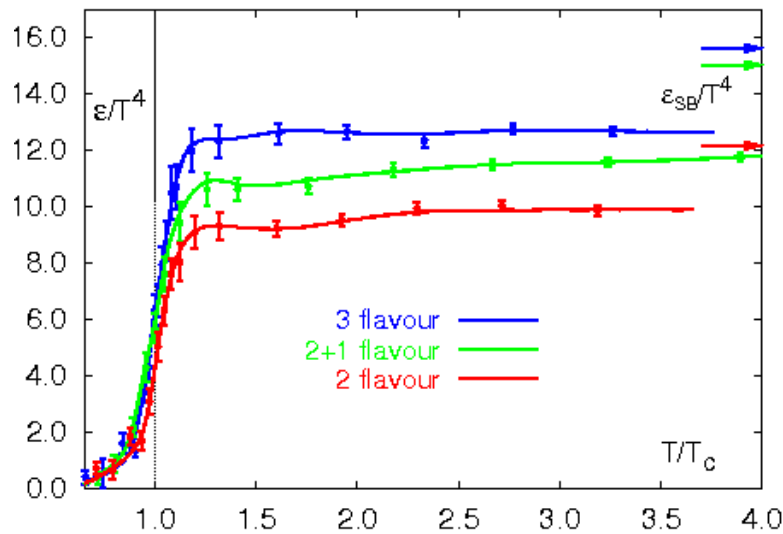


Figure 1.1 Results from lattice QCD [7] for the energy density/ T^4 as a function of T/T_c .

At the beginning of the universe, μs after the “Big Bang” such a state

¹David J. Gross, H. David Politzer and Frank Wilczek have been awarded with the Nobel Prize in Physics in 2004 for the discovery of asymptotic freedom in the theory of the strong interaction [2, 3] and [4]

existed before the universe cooled down and expanded further. During the expansion the strong interaction force increased and confined the quarks and gluons to hadrons. The RHIC experiment was designed to recreate a QGP with low baryon densities. A phase diagram is shown in Fig. 1.2.

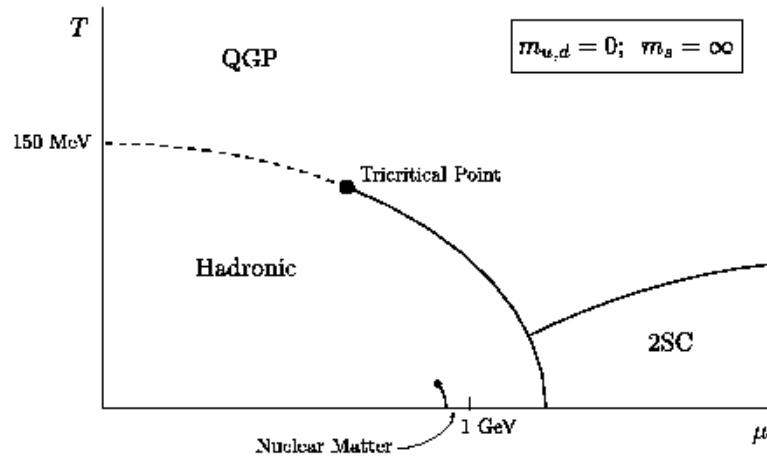


Figure 1.2 Theoretical phase diagram as a function of temperature and baryon chemical potential. [8].

Since the first data from Au + Au collisions at RHIC were taken, there was a large effort to find evidences of the QGP. However, due to the confinement of quarks and gluons after the hadronization process one has to rely on indirect observables that prove the creation of a QGP in Au+Au collisions. A summary of the present accomplishments can be found in the PHENIX Whitepaper [8].

1.2 Thermal Photons

In order to obtain information from the earliest and hottest stage of the QGP, direct photons are a very promising signature [9]. Because they do not interact strongly they escape the medium unaffected of final state interactions. Thermal photons are emitted like black body radiation from QGP. Microscopically, the main production mechanisms are quark-gluon Compton scattering $gg \rightarrow \gamma q$, quark-antiquark annihilation $q\bar{q} \rightarrow \gamma g$ and bremsstrahlung [10] involving thermalized partons. Other sources of direct photons are also produced in initial hard scattering processes which involve the same reactions but among the incoming particles.

A calculation for RHIC energies has been done in [9] which predicts a p_T window for thermal photons at 1–3 GeV/c (see Fig. 1.3).

The first measurement of direct photons in ultra-relativistic heavy-ion collisions has been made at the CERN WA98 experiment at SPS [11]. The result is shown in Fig. 1.4. Direct photons have been found to be present at the 10 % most central events of Pb + Pb collisions in the p_T range above 1.5 GeV/c.

Also at PHENIX direct photons have been measured in Au + Au collisions at $\sqrt{s_{NN}} = 200$ GeV [12]. In Fig. 1.5 a double ratio of the measured γ over π^0 ratio and the background γ over π^0 ratio is shown. The background was calculated by simulations and the division by π^0 spectra was done to cancel

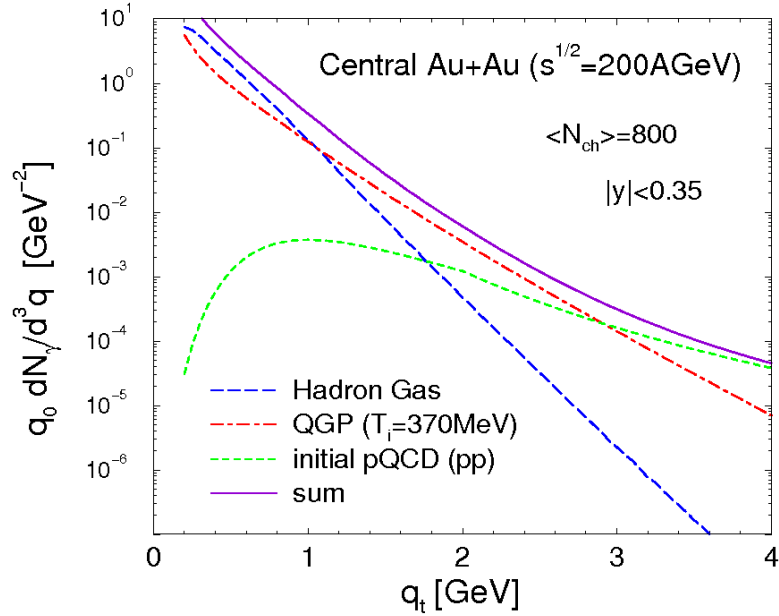


Figure 1.3 Integrated photon emission spectra from central Au + Au collisions at RHIC. Short-dashed line (green): pQCD photons from primordial N - N collisions; dashed-dotted line (red): thermal QGP radiation; long-dashed line (blue): thermal hadron gas emission; solid line (purple): total direct photon yield.[9]

certain systematic errors. An excess > 1 is interpreted as the direct photon contribution.

This is a convincing result for the presence of direct photons in Au + Au collisions. However, in the p_T region around 2 GeV/ c the systematic error of $\approx 30\%$ does not allow a final conclusion whether there is a thermal photon contribution.

This thesis introduces a new method of photon measurements with PHENIX.

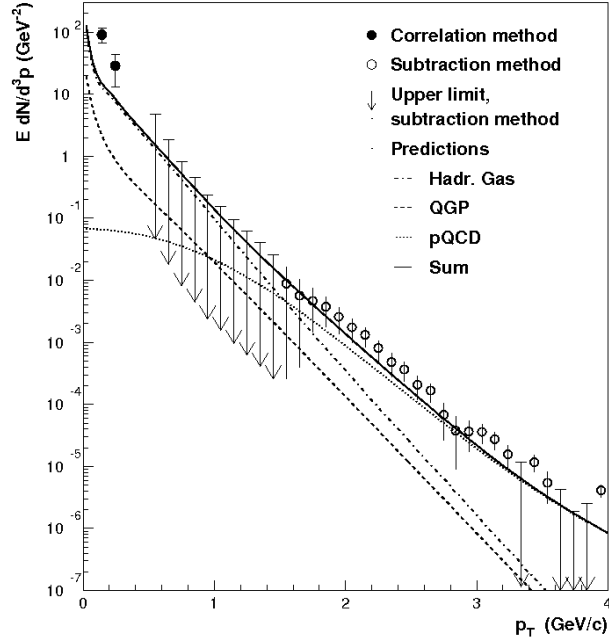


Figure 1.4 Measurement of direct photons at WA98 [11].

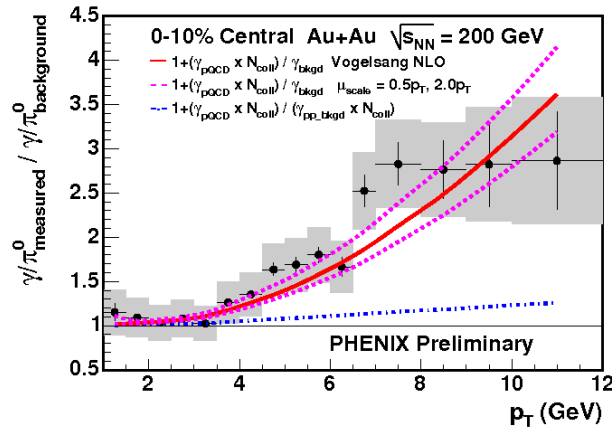


Figure 1.5 Photon excess double ratio for the most central Au+Au bin, compared to pQCD [33] for different scale factors as indicated. [12].

In contrast to former analyses, we do not measure the photons themselves but e^+e^- -pairs from beam pipe conversions. The PHENIX detector enables us to measure e^+e^- -pairs with high accuracy in the momentum range from 1–3 GeV/c.

Chapter 2

The PHENIX Experiment

The PHENIX experiment is one of the four experiments at the Relativistic Heavy Ion Collider (RHIC) which is located at the Brookhaven National Laboratory (BNL). RHIC was built to analyze the early state of the universe to find evidences of the quark gluon plasma in Au + Au collisions. The PHENIX detector was designed to measure hadrons, leptons and photons with high momentum and good energy resolution. PHENIX consists out of several subsystems which can be classified in three categories:

- Global Detectors
- The Central Arms
- The Muon Arms

The Global Detectors measure time and position of Au + Au collision and the multiplicity of the events.

The two Central Arms cover a rapidity range of ± 0.35 and each of them covers each an azimuthal angle of 90° . They contain subsystems to measure photons and electrons as well as hadrons. In the PHENIX coordinate system they are called west and east arm.

The Muon Arms are at forward positions and cover the full azimuthal angle. As their name implies these detectors measure muons. The north arm reaches from $\eta = 1.1$ to $\eta = 2.4$ and the south arm from $\eta = -1.1$ to $\eta = -2.2$. Since they are not used in the analysis they will not be explained in more detail. For further information see [13].

In the PHENIX coordinate system the beam pipe is parallel to the z-axis which points into the north muon arm. The x-axis points horizontally towards the west arm. Thus the y-axis points in upward direction.

In Fig. 2.1 you can see the detector configuration which was used to take the data this analysis is based on. The upper picture is a cutaway perpendicular to the beam pipe and shows the subsystems of the central arms. The Drift Chamber is the closest detector to the beam pipe. It is followed by the Pad Chamber 1 and the RICH. In the west arm the Pad Chamber 2, the Aerogel detector and the Pad Chamber 3 follow towards larger radii. The

Pb-scintillator (PbSc) Electromagnetic Calorimeter is the outermost detector. There is no Pad Chamber 2 in the east arm but the Time Expansion Chamber, the Pad Chamber 3 and the Time of Flight detector. The east arm has two different types of Electromagnetic Calorimeters, the upper two units are PbSc as in the west arm and the two lower units are Pb-glass (PbGl) calorimeters.

The lower picture shows a cutaway along the beam pipe with the Central Magnet in the center. Going towards the north side you can see first the Beam Beam Counter and the north muon magnet including the Muon Trackers followed by the Muon ID detector and the Zero Degree Calorimeter. The order of the detectors in south direction is the same.

2.1 Global Detectors

The global parameters of an Au + Au collision are measured by the BBC (Beam-Beam Counters) and the ZDC (Zero Degree Calorimeter). These parameters are the vertex position in z-direction, the collision time and the multiplicity. Furthermore it is possible to reconstruct the reaction plane and the centrality of an event with these global detectors.

The ZDCs [14],[15] are small hadron calorimeters with a total width of only 10 cm which are installed at all four RHIC experiments. The purpose is to detect spectator neutrons which travel along the beam pipe and to measure

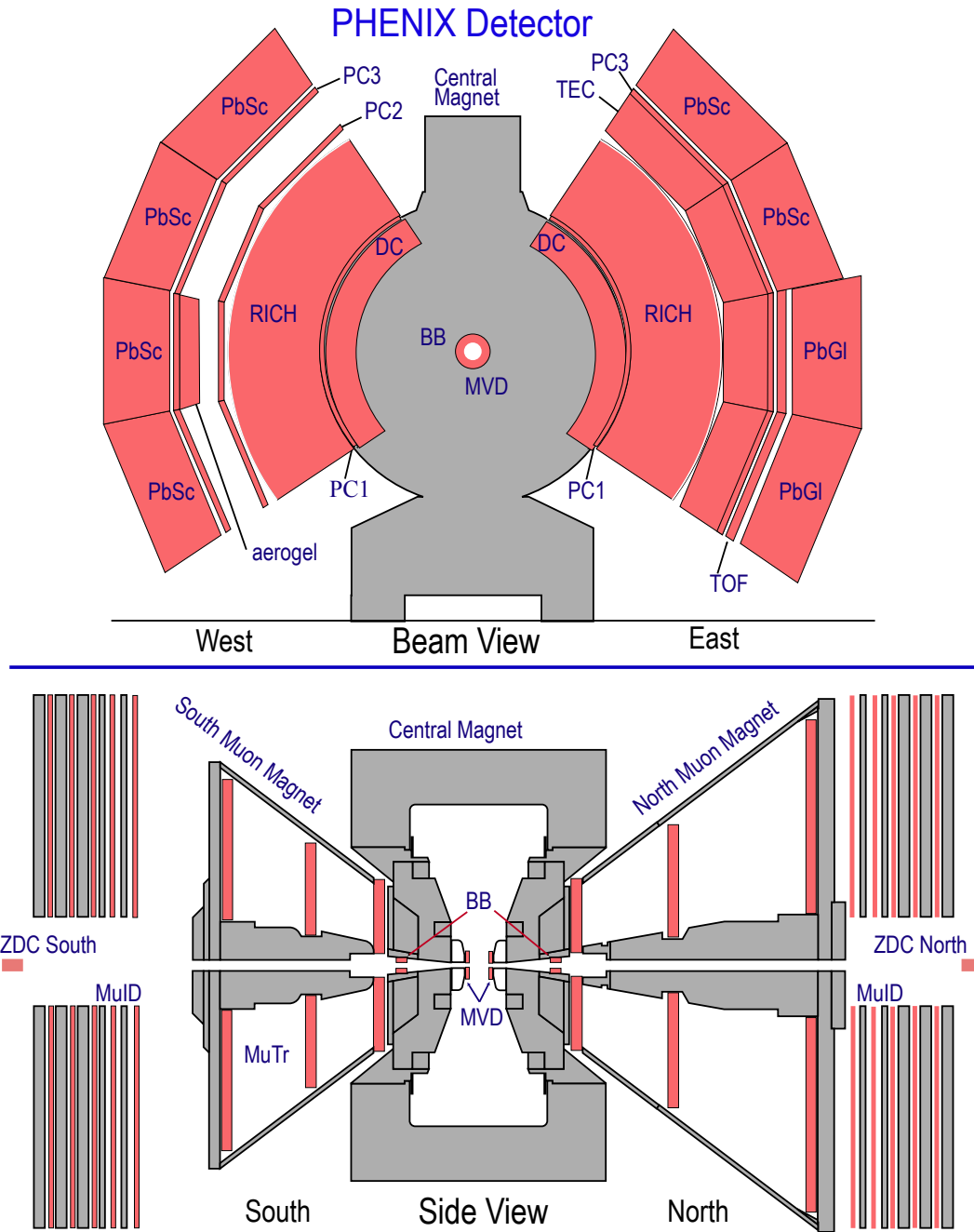


Figure 2.1 PHENIX Detector configuration during Run 04. The upper picture shows the central arm in a plane perpendicular to the beam pipe, whereas the lower figure the detector arrangement along the beam pipe displays.

their total energy (multiplicity). They are placed 18 m up and downstream the beam pipe behind the beam bending magnets so charged particles like protons will be deflected out of the acceptance before they can hit the ZDC. The ZDC coincidence of the two beam directions is a minimal bias¹ selection of mutual beam interactions. This makes it useful as an event trigger and a luminosity monitor. The neutron multiplicity is also known to be correlated with event geometry

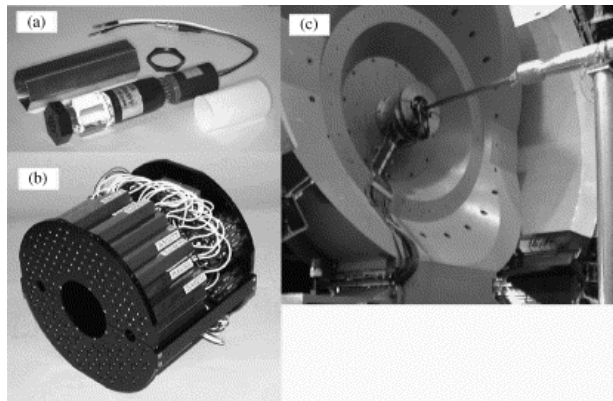


Figure 2.2 The Beam-Beam Counters.

The main role of the BBC [16] is to provide information about the collision time for the ToF and to measure the collision vertex point (z_{vtx}). They are two identical arrays of 64 Cherenkov radiators which are read out by photo multiplier tubes. They are placed at 1.44 m away from the interaction point

¹Every trigger to select collision events will bias the data sample. The term minimal bias describes the selection with the smallest possible error.

surrounding the beam pipe (see Fig. 2.2); that corresponds to a pseudo rapidity range of 3.0 to 3.9 over the full azimuth. In contrast to the ZDC, the BBC is sensitive to charged particle produced in the collision

2.2 The Central Arm

The detectors in the central arms are designed to track charged particles, measure their momentum and are used for particle identification. The subsystems of the central arm have different tasks and are introduced in the following.

2.2.1 The Central Arm Magnet

The Central Arm Magnet [17] produces a high magnetic field which is parallel to the beam pipe to bend charged particles in azimuthal direction and enable the momentum reconstruction in the Drift Chamber.

There are three major requirements for the Central Arm Magnet:

- No mass in the central arm detector aperture to minimize multiple scattering and interactions with particles from the collision vertex.
- Low magnetic field integral in the region of the Drift Chamber and the RICH to minimize errors in the track reconstruction and ring association.

- Control over the magnetic field strength to run with zero field configuration

For the latter requirement there are two sets of circular coils in the central magnet pole face (see Fig. 2.3) which can be run with two different configurations (adding “++” or bucking “+-”). In the bucking mode the fields cancel so the magnetic field integral for the region $0 < R < 50$ cm is approximately zero.

This analysis was based on data taken during the “++” configuration.

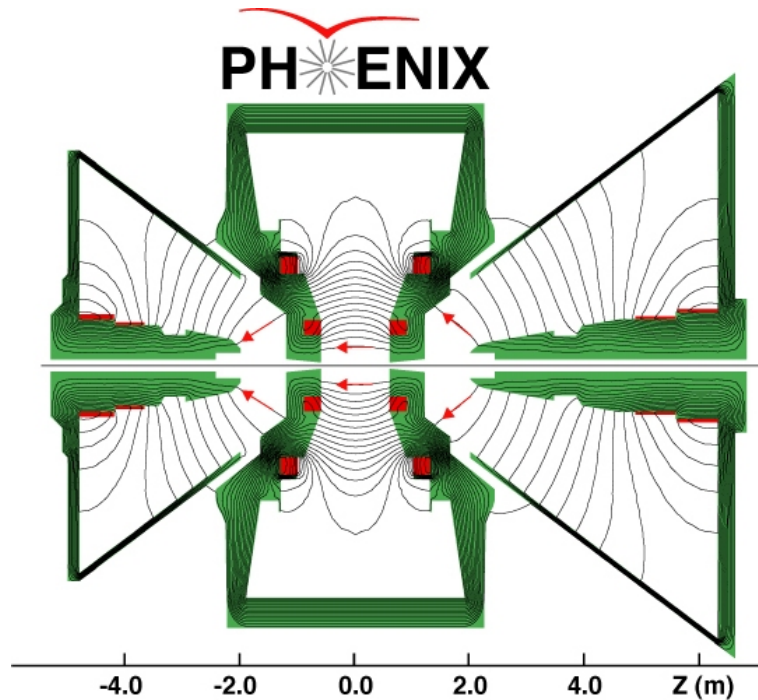


Figure 2.3 Magnetic field lines for the two Central Magnets in the combined “++” mode.

2.2.2 The Drift Chambers

The Drift Chambers [18] are designed to provide the following functionalities:

- Measure trajectories in the $r - \varphi$ plane and determine the p_T of charged particles.
- Provide z-position information together with the Pad Chambers and determine the track's polar angle θ with the help of the z_{vtx} information from the BBC.
- Help to connect the information from the different subsystems to particle tracks.

To achieve this the Drift Chambers have to fulfill a list of requirements:

- Single wire resolution better than $150\mu\text{m}$ in $r - \varphi$.
- Single wire two track separation better than 1.5 mm.
- Single wire efficiency better than 99 %.
- Spatial resolution in the z-direction better than 2 mm.

The Drift Chambers are two independent gas volumes in the east and the west arm. Their volume is defined by a titanium frame shown in Fig. 2.4 which has an extension of 2 m along the beam direction and reaches from 2 to 2.4 m

in radial direction. The Drift Chambers are operated with a mixture of 50 % Argon and 50 % Ethane.

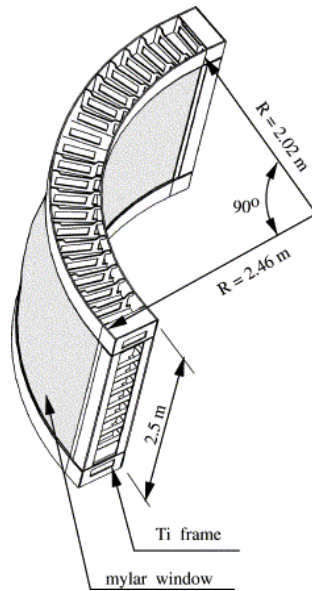


Figure 2.4 DC frame [18].

Each frame is divided into 20 equally sized sections which cover an azimuthal angle of 4.5° each. Each sector contains four cells with six units of different wire types in the following order: X1, U1, V1, X2, U2, V2. X1 and X2 wires are aligned parallel to the beam pipe for $r - \varphi$ measurements. The U and V stereo wires have an angle of $\approx 6^\circ$ towards the X wires, so they provide information about the z-position of a track together with the Pad Chambers. The angle was chosen to match the Pad Chamber z resolution and minimize track ambiguities. Each sector contains 12 X and 4 U,V anode wires each. The

wire layout is shown in Fig. 2.5. The back and gate wires focus the electric field lines to eliminate the left-right ambiguity.

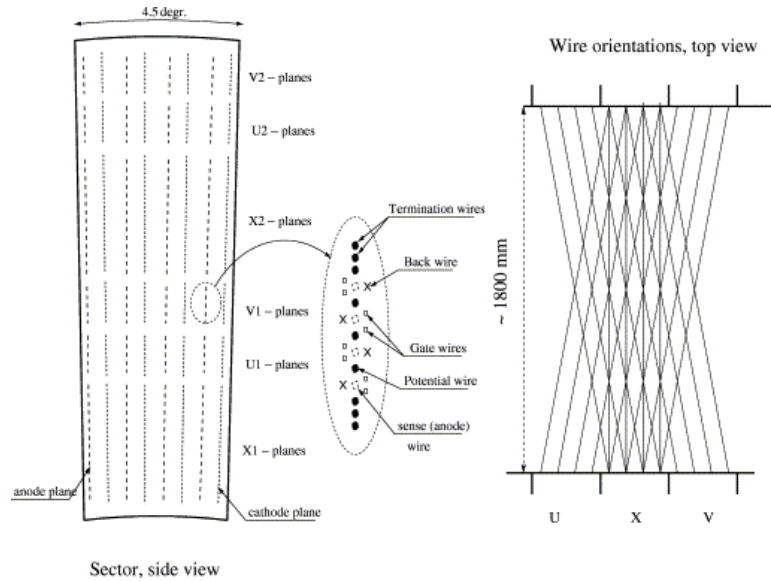


Figure 2.5 The layout of wire position within one sector and inside the anode plane (left). A schematic diagram, top view, of the stereo wire orientation (right) [18].

The sense wires were separated in two halves to satisfy the requirements of efficient track recognition even for high track numbers (≈ 500) as they are expected in central Au + Au collisions. So the electrical read out of the north and the south wires is done independently.

Fig. 2.6 shows how the momentum reconstruction is done with the Drift Chambers. The angle α between the reconstructed particle trajectory and a line which connects the collision vertex point with the particle trajectory at the reference radius $R = 220$ cm is proportional to charge/ p_T . So an electron

with infinitely high momentum would be reconstructed with an angle $\alpha = 0$ and a low p_T particle is reconstructed with a large angle α .

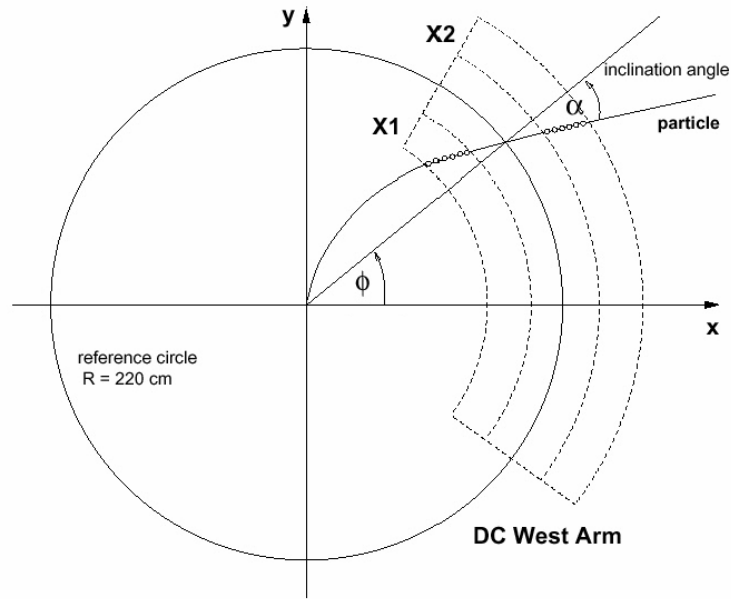


Figure 2.6 The angle α is measured in the Drift Chamber. This angle is proportional to charge/ p_T .

2.2.3 The Pad Chambers

The Pad Chamber system [18] is the second subsystem which provides particle tracking information. It determines space points along straight line particle trajectories outside the magnetic field.

The innermost Pad Chamber called PC1 is located between the Drift Chamber and the RICH. In the west arm the PC2 is mounted behind the

RICH and the PC3 follows in both arms right before the Electromagnetic Calorimeters.

Due to their non-projective nature the Pad Chambers are important elements for the pattern recognition. Furthermore, PC1 is used to determine the three-dimensional momentum vector by providing information about the z coordinate at the exit of the Drift Chamber.

They are also used as charged particle veto in front of the Electromagnetic Calorimeter and to distinguish electrons from other particles by accurate pointing of charged tracks to the RICH and Electromagnetic Calorimeter.

The design of the Pad Chambers was driven by several performance and spatial constraints:

- Low occupancy in spite of a high charged particle multiplicity.
- High efficiency and reliable hit information.
- Good position resolution in the z direction.
- Low mass to minimize multiples scattering and secondary particle production.

The Pad Chambers are multiwire proportional chambers which contain each a single plane of wires inside a gas volume bounded by two cathode planes. One cathode is finely segmented into an array of pixels (see Fig. 2.7).

The charge induced on a number of pixels when a charged particle starts an avalanche on an anode wire is read out through specially designed readout electronics.

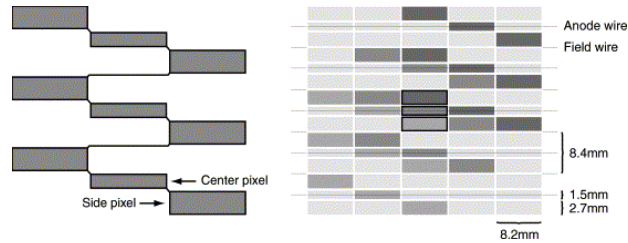


Figure 2.7 The pad and pixel geometry (left). A cell defined by three pixels is at the center of the right picture [18].

2.2.4 The RICH

The Ring-Imaging Cherenkov [19] provides identification of charged particles for the PHENIX central arm. The RICH is located between the inner and outer tracking units in both arms. Fig. 2.8 contains a cutaway drawing of one of the RICH detectors revealing the internal components. Each RICH detector has a volume of 40 m^3 , with an entrance window area of 8.9 m^2 and an exit window area of 21.6 m^2 . The spherical mirrors focus Cherenkov light onto two arrays of photo multiplier tubes, each located on either side of the RICH entrance window.

The detector provides e/π discrimination below the π Cherenkov threshold,

which is for the used gas (CO_2) 4.5 GeV/c. With the current setup a hadron rejection factor of 1/300 is achieved.

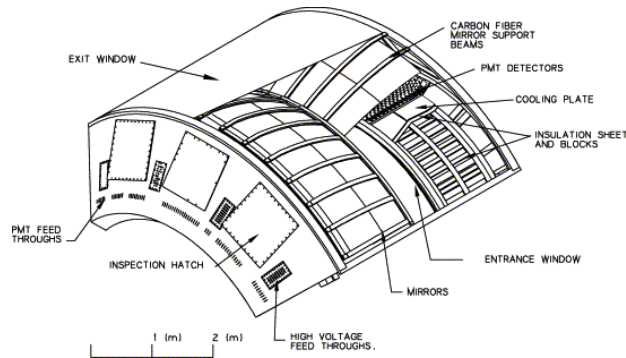


Figure 2.8 A cutaway view of one arm of the PHENIX RICH detector [19].

2.2.5 The Electromagnetic Calorimeters

The Electromagnetic Calorimeters [20] in the PHENIX detector are used to measure spatial position and energy of electrons and photons. PHENIX is using two different types of calorimeters, in the west arm all four sectors are PbSc calorimeters, which are sampling calorimeters. In the east arm the two upper sectors are PbSc calorimeters as well, while the lower half of the arm is equipped with PbGl, a Cherenkov detector. Both detector types provide a very good energy, spatial position and timing resolution.

In total the EMCal system consists out of 24,768 individual detector modules. Each PbSc module is made of four towers (shown in Fig. 2.9 which

contains 66 sampling cells – alternating tiles of Pb and scintillator. Phototubes at the back of each tower read out the produced light. PbG1 modules are comprised to a supermodule in groups of 24.

The EMCal is mainly designed for direct photon measurements, electron identification and neutral meson measurements via their $\gamma\gamma$ decay channel.

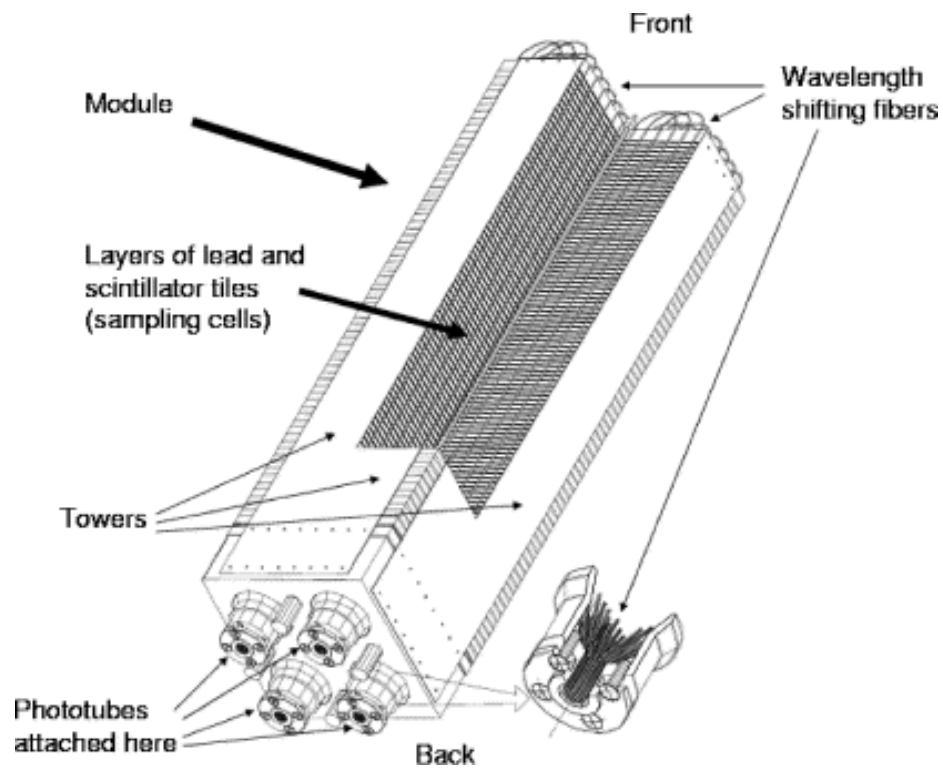


Figure 2.9 Cutaway of the PbSc calorimeter module [20].

Chapter 3

Analysis

The basic idea of this analysis is to reconstruct photons which converted in the material of the beam pipe into e^+e^- -pairs. The way electron tracks are reconstructed in the PHENIX detector lets beam pipe conversions appear as a peak at 20 MeV/c in an e^+e^- -pair mass spectrum. This enables a clean identification of these conversion electrons down to a momentum cutoff at 150 MeV/c.

3.1 Dataset and Run Selection

This analysis is based on the data reconstructed from Au + Au collisions at $\sqrt{s_{NN}} = 62.4$ GeV collected during the run in year 2004.

The list of used runs can be found in App. A. The analyzed data files passed the online minimum bias trigger threshold, which requires that two

photo tubes are hit both in BBC north as well as the BBC south.

We only selected events inside these runs which fulfilled the following requirements:

- Minimum Bias event (BBC north and south have both at least 2 fired photo tubes)
- BBC z vertex $\leq 25\text{cm}$

About 31.4 million events passed this event selection criteria.

3.2 Electron Identification

The first step in order to identify photon conversions in the beam pipe is to select electrons from all produced particles in each event. To accomplish this we can use the different detector subsystems.

We begin by requiring a charged particle which fulfills certain quality criteria. For our analysis we require a track quality of 63, 51 or 31. These numbers represent bit patterns which have the following meaning (a complete list of all bit patterns can be found in Tab. 3.2):

- 63: Hits in the X1 and X2 wires of the DC as well as unique hits in the UV stereo wires and a unique PC1 choice.

- 51: Hits in the X1 and X2 wires of the DC as well as unique hits in the UV stereo wires and more than one choice in PC1.
- 31: Hits in the X1 and X2 wires of the DC but no hits in the UV stereo wires and more than one choice in PC1.

meaning	PC1 unique	PC1 found	UV unique	UV found	X2 used	X1 used
bit position	5	4	3	2	1	0
decimal value	32	16	8	4	2	1

Table 3.1 Available bits to characterize the hit quality

49, 50, 51	1 1 0 0 x x	PC1 found/unique, no UV
61, 62, 63	1 1 1 1 x x	PC1 found/unique, UV found/unique
17, 18, 19	0 1 0 0 x x	PC1 found/ambiguous, no UVs
21, 22, 23	0 1 0 1 x x	PC1 found/ambiguous, UV found but tied
29, 30, 31	0 1 1 1 x x	PC1 found/ambiguous, UV found w/ one best choice

Table 3.2 List of valid bit patterns for the DC track quality [21]

In the next step we limit our number of electron candidates by a momentum cut. To eliminate electrons created by conversions in the detector material, e.g. the Drift Chamber frame, we used an upper threshold of 20 GeV/c. Electrons which are created close to the Drift Chamber are not bent in the magnetic

field which leads to $\alpha \approx 0$. Since $\alpha \sim \frac{1}{p_T}$ this leads to an wrong and too large momentum. Moreover we set a cut on low momentum tracks at 150 MeV/c. Electrons with lower momentum would be bend too strong by the magnetic field and would not reach the detector arms.

To clean the sample of tracks from hadronic background we use information from the RICH detector.

- $n0 \geq 3$: The number of fired photo tubes within the association area around the track.
- $n3 \geq 1$: Number of photo tube in the same area as $n0$ but with additional timing requirement.
- $disp < 5$: Displacement of the ring center with respect to the track projection
- $\chi^2/npe0 < 10$: χ^2 is in units of cm^2 for the ring shape and $npe0$ is the number of photoelectrons summed over the ring area

Due to the low mass of the electron the energy it deposits in the Electromagnetic Calorimeter is as big as its momentum measured by the Drift Chamber. So the ratio of shower energy and momentum is equal to one but smeared with a Gaussian due to the limited energy resolution of the Electromagnetic Calorimeter at low p_T ; and at high p_T due to the momentum

resolution of the Drift Chamber.

$$\frac{\sigma_{p_T}}{p_T} = \sqrt{0.8\ \%^2 + (p_T \cdot 0.91\ \%)^2} \quad (3.1)$$

$$\frac{\sigma_E}{E} = 0.8\ \% + \frac{5.9\ \%}{\sqrt{E}} \quad (3.2)$$

So we cut in range of $0.7 \leq E/p \leq 2.0$ and require as a last cut a 5σ matching either in PC3 or in the Electromagnetic Calorimeter.

3.3 Monte Carlo Simulations

For this analysis we simulated 10 million π^0 decays with EXODUS, which is a phenomenological event generator that allows to simulate the phase space distribution of relevant electron and e^+e^- -pair sources [22]. These π^0 decays are simulated flat in a rapidity range of $-0.6 < y < 0.6$, an azimuthal range $0 < \varphi < 2\pi$ rad and flat in p_T from 0 to 10 GeV/c. The tracking of the generated particles and their decay product is done with the PHENIX detector model which is described in PISA (PHENIX Integrated Simulation Application) a GEANT-3 [39] based simulation code [23]. Afterwards these events pass through the same track reconstruction algorithms as is used for real event data.

In order to get a realistic p_T distribution we used the preliminary π^0 p_T spectrum for $\sqrt{s_{NN}} = 62.4$ GeV minimum bias from PHENIX Analysis Note 292 [24] shown in Fig. 3.1.

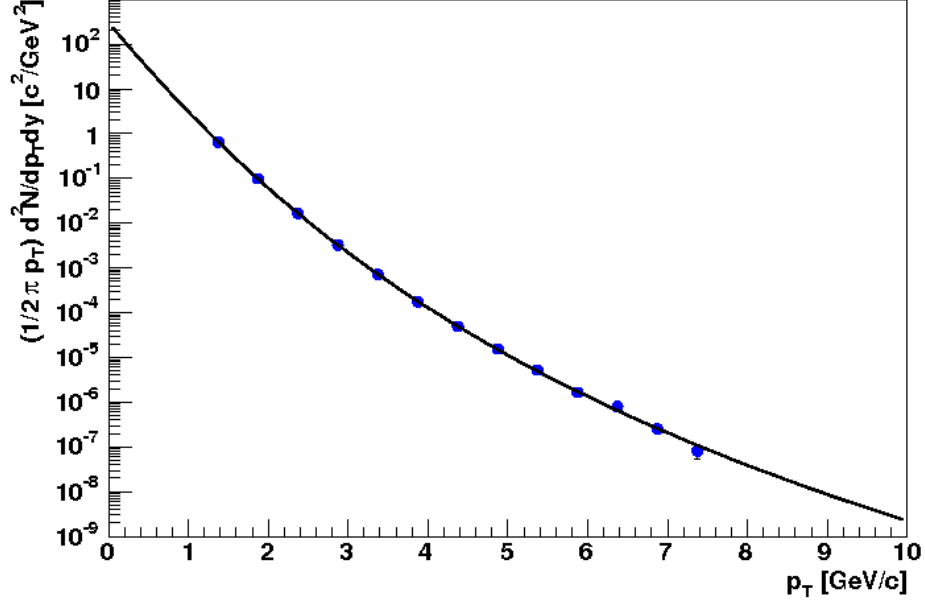


Figure 3.1 Preliminary π^0 p_T spectrum [24].

A fit of this spectrum with a function of the form:

$$f(p_T) = \frac{A}{(e^{a p_T} + p_T/p_0)^n} \quad (3.3)$$

gives the following parameters:

$$A = (302.2 \pm 374.9) \text{ c}^2/\text{GeV}^2$$

$$a = -0.317 \pm 0.1919$$

$$p_0 = (1.561 \pm 0.204) \text{ GeV}/c$$

$$n = 13.28 \pm 1.62$$

The large errors can be explained with the big p_T range we fit. The function

covers 13 orders of magnitude in the simulated p_T range. The reduced χ^2 is 3.827/9.

The fit result is used as a weighting function for the Monte Carlo simulation whenever we compare it to the real data. It is important to notice that the fit is done for a spectra $\frac{1}{p_T} \frac{dN}{dp_T}$ as where many plots in the following will have the form of $\frac{dN}{dp_T}$. We will take this additional factor p_T into account when we weight such distributions.

Due to the low conversion probability in the beam pipe ($P \approx 0.2\%$)

$$P = 1.0 - \exp(-7/9 \cdot x/X_0) \quad (3.4)$$

$$x = 0.3\% \cdot X_0$$

most of the simulated events will not result in a detectable e^+e^- -pair. Therefore we produced a second modified Monte Carlo simulation with larger conversion probability. We could not just change the beam pipe material (e.g. Pb or U) to decrease the radiation length, because that would increase the conversion probability on the one hand, but on the other hand it would also increase multiple scattering. So instead we went back to the very beginning of the simulation process and decreased the average path length to the next pair production process for Be by a factor of 20. At the same time we changed the branching ratio of the π^0 Dalitz decay to keep the ratio between Dalitz pairs and conversion pairs constant. The branching ratio for the two Monte Carlo

simulations are as follows:

	original	modified
$\pi^0 \rightarrow \gamma \gamma$	98.802 %	76.04 %
$\pi^0 \rightarrow \gamma e^+e^-$	1.198 %	23.96 %

As we will discuss in Section 3.5, we will take into account the differences between these two simulations by an extra correction factor.

Fig. 3.2 shows α as a function of φ as a comparison of electrons generated with the Monte Carlo simulations and the real data. This plot represents the active area of the Drift Chamber in simulation and real data. For comparison we use the same electron identification cuts and scale the Monte Carlo simulation with the ratio of the real data's integral and the simulation's integral.

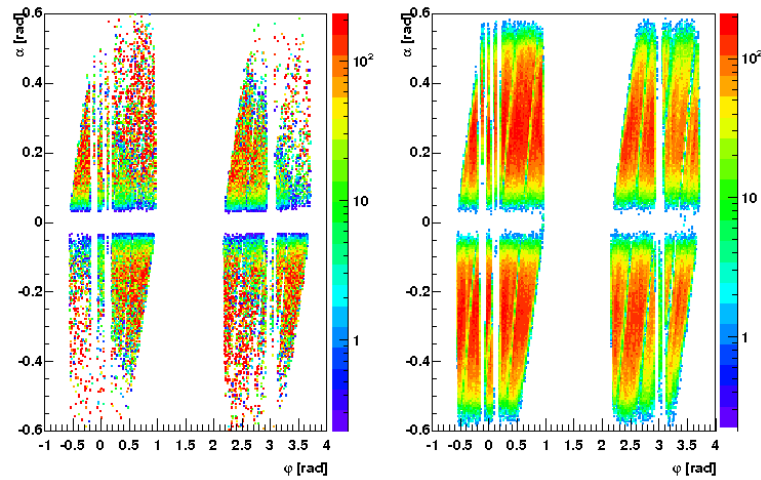


Figure 3.2 Comparison of the active area between Monte Carlo Simulation and real data.

Besides the nice separation between the west ($\varphi < 1.5$ rad) and the east arm ($\varphi > 1.5$ rad) you can see two kind of structures in the detector acceptance. The vertical ones originate from deactivated keystones in the Drift Chamber. Due to the short run period with 62.4 GeV we were rather interested in more stable acceptance than in a higher but varying acceptance. The diagonal stripes are from the structure of the Electromagnetic Calorimeter. The borders between two sectors are projected as diagonals onto the Drift Chamber acceptance. For a given φ which is a fixed point at the Drift Chamber α runs over the EMCal and hits for certain values of α a sector edge. These values depend linear on φ which leads to the diagonal stripes in the acceptance plot.

In this figure there are two areas of disagreement between the Monte Carlo Simulation and the real data. For small α and small φ as well as for large α and large φ there are wholes which are not understood entirely. We take this into account in the systematic uncertainties.

3.4 e^+e^- -pairs

Once we have found all electrons in one event we can go ahead and combine them to pairs. One can imagine that we get two groups of pairs like sign pairs (electron – electron or positron – positron) and unlike sign pairs (electron – positron), respectively.

For each combination of electrons and positrons we calculate their invariant mass which is the mass of their parent particle. $m_{inv}^2 = (p_{e^+} + p_{e^-})^2$ with p_{e^+} , p_{e^-} representing the 4-momentum vector of the positron and the electron, respectively.

An invariant mass spectra up to $0.1 \text{ GeV}/c^2$ is shown in 3.3. In this spectrum you can see three major components, first the very clear peak at $5 \text{ MeV}/c^2$ with its decreasing yield towards higher masses which comes from Dalitz decays $\pi^0 \rightarrow \gamma e^+ e^-$. Due to the momentum cut at $150 \text{ MeV}/c$ for the electrons we observe a cutoff in the increasing Dalitz spectrum at low masses. There is a second dominant peak at $20 \text{ MeV}/c^2$ on top of the Dalitz decays. This peak is caused by γ conversions $\gamma \rightarrow e^+ e^-$ in the beam pipe. These γ have two sources, meson decays like $\pi^0 \rightarrow \gamma\gamma$ and direct photons. It is the goal of this analysis to extract this peak from all other e^+e^- -pairs. Towards higher masses the pairs are created by γ conversions in the air between the beam pipe and the PHENIX detector arms. The next section will explain in detail the origin of the invariant mass of γ conversion pairs.

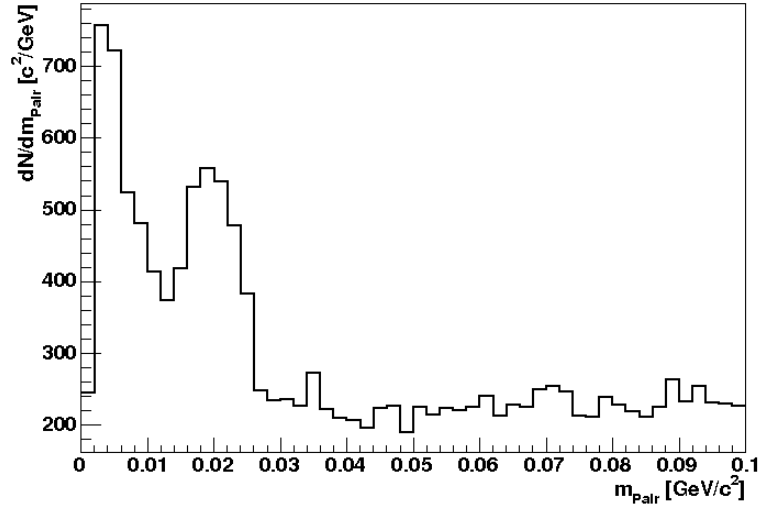


Figure 3.3 Invariant mass spectrum of e^+e^- -pairs . The peak at $20 \text{ MeV}/c^2$ comes from photon conversions in the beam pipe material. The Dalitz decays peak at lower masses and have a tail up to the π^0 mass of $134 \text{ MeV}/c^2$. At higher masses there air conversions and combinatorial background start to dominate the spectrum.

3.4.1 Photon Conversions in PHENIX

Conversions from real photons as we are interested in do not have an invariant mass. The fact that we see γ conversions in PHENIX at invariant masses different from $0 \text{ MeV}/c$ is due to the way we reconstruct electrons in PHENIX.

The transverse momentum of a charged particle is measured in the PHENIX drift chamber. As mentioned in Chapter 2 we can measure the angle between the track of a charged particle which was bent in the magnetic field and the

reference radius. This angle α is proportional to charge/ p_T .

In the case of beam pipe conversions we have a photon emerging from the collision vertex and penetrating the beam pipe. The beam pipe has a radius of ≈ 4 cm. With a conversion probability of 0.2 % there will be an e^+e^- -pair created which will be detected in the detector if the electron and the positron are within the acceptance. In contrast to the photon the electrons will be bent by the magnetic field produced by the central arm magnets. This magnetic field has a direction parallel to the beam pipe which means in the PHENIX coordinate system only a \vec{z} component. This has two effects on the e^+e^- -pair which will be explained in the following:

- The pair obtains an artificial azimuthal opening angle
- The electron's transverse momentum is improperly reconstructed

The electron's p_T is improperly reconstructed because the reconstruction algorithm traces back the origin of the electron to the collision vertex. For a given α in the drift chamber the angle reconstructed azimuthal angle at the collision vertex φ_0^{reco} is always larger than the real azimuthal angle φ_0^{true} in conversion vertex (see Fig. 3.4). For the positron we observe the opposite effect φ_0^{reco} is always smaller than φ_0^{true} .

This causes the reconstructed p_T to be larger than the real p_T , because

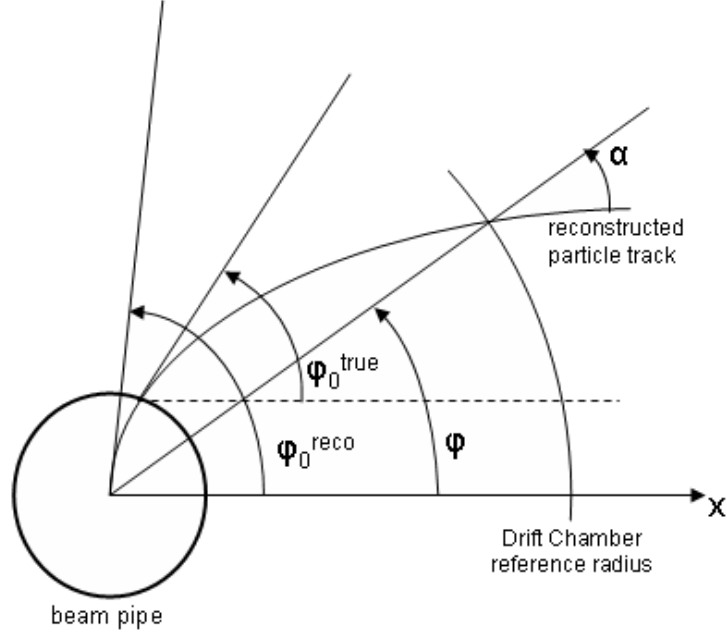


Figure 3.4 Track reconstruction in the Drift Chamber. For a given α in the DC the reconstructed angle φ_0^{reco} of a particle which was created in the beam pipe is larger than the true azimuthal angle φ_0^{true} .

the electron was assumed to travel through the magnetic field integral further than it really did.

$$\int_0^{\infty} B dl > \int_{r_{b.p.}}^{\infty} B dl \Rightarrow p_T^{reco} > p_T^{true} \Rightarrow m_{inv}^2 > 0 \quad (3.5)$$

Due to this higher p_T , the e^+e^- -pair acquires an additional mass which is to first approximation proportional to the distance from the origin of the PHENIX coordinate system.

$$m_{inv}^2 = (p_{e^+} + p_{e^-})^2 \quad (3.6)$$

$$\begin{aligned} &= (E_{e^+} + E_{e^-})^2 - (\vec{p}_{e^+} + \vec{p}_{e^-})^2 \\ &= E_{e^+}^2 + 2 E_{e^+} E_{e^-} + E_{e^-}^2 - \vec{p}_{e^+}^2 - 2 \cdot \vec{p}_{e^+} \cdot \vec{p}_{e^-} - \vec{p}_{e^-}^2 \\ &= 2 \|\vec{p}_{e^+}\| \cdot \|\vec{p}_{e^-}\| (1 - \cos \vartheta) \end{aligned}$$

$$m_{inv} = \sqrt{2} \langle p \rangle \sin \frac{\vartheta}{2} \quad (3.7)$$

We can distinguish two different constellations of e^+e^- -pairs we detect in PHENIX (see Fig. 3.5). For the first, the conversion photon has a low p_T . The pair splits up with a large opening angle so that the electron hits one arm and the positron the opposite arm. These events are due to there small acceptance in PHENIX rare compared two the other case: both particles – the electron and the positron – hit the same arm, either the west or the east arm. In this analysis we focus only on these kinds of events limiting the photon p_T range to above $0.8\text{GeV}/c$. A future analysis of the low p_T photon conversions may be able to measure a photon p_T spectrum down to $400\text{MeV}/c$, see Fig. 3.6.

In the following we will strictly separate between e^+e^- -pairs which hit the west arm and the pairs which hit the east arm. We do this for several reasons. The most important one is that the conversion peak has slightly different apparent masses in the invariant mass spectrum (see Fig. 3.12). The reason

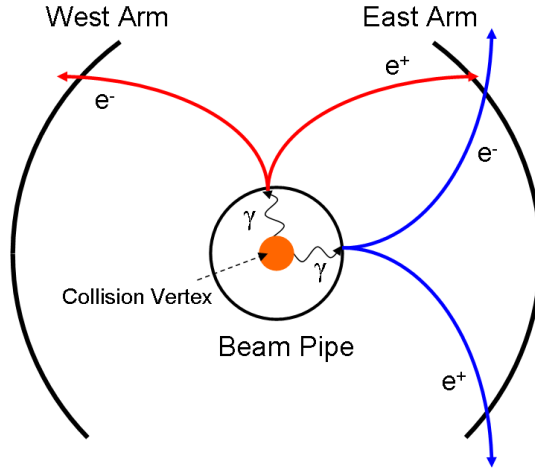


Figure 3.5 There are two ways e^+e^- -pairs can hit the PHENIX detector arms. The red e^+e^- -pair hits both detector arms as where the blue e^+e^- -pair is measured in one arm.

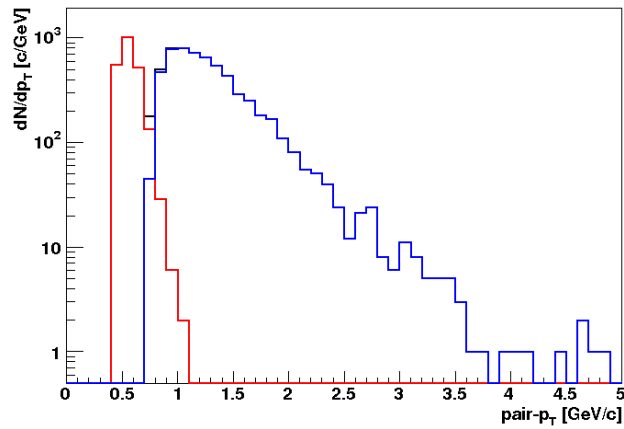


Figure 3.6 e^+e^- -pairs p_T spectrum. In red you can see e^+e^- -pairs where the electron hit a different arm than the positron. In blue you can see e^+e^- -pairs where electrons and positrons hit the same arm. The black line is the sum of red and blue.

is that the beam axis and the center of the beam pipe are not the same. The beam axis is determined by the track origins in zero field runs, whereas the beam pipe is fixed and has an independent center.

Furthermore we can calculate the geometry of the pair, e.g. its azimuthal and polar direction or the opening angle which is the angle between the momentum vector of the electron and of the positron.

$$\xi_{Pair} = \arccos\left(\frac{\vec{p}_{e^+} \cdot \vec{p}_{e^-}}{\|\vec{p}_{e^+}\| \cdot \|\vec{p}_{e^-}\|}\right) \quad (3.8)$$

This information is important to isolate beam pipe conversions from other electron pair sources as Dalitz decays $\pi^0 \rightarrow \gamma e^+e^-$.

3.4.2 Pair Cuts

Once we have an invariant mass spectrum of e^+e^- -pairs we extract the peak from beam pipe conversions. For this, we have to find properties which distinguish Dalitz decays from conversion pairs.

The major difference between Dalitz decays and conversion pairs is their opening angle. The photon conversions have only a small opening angle because a photon doesn't have a mass which can contribute to the opening of the pair. This means that the electron and the positron fly in almost the same direction as their parent photon did. Whereas the π^0 has a mass which can open the e^+e^- -pair with an arbitrary orientation in space. Once the e^+e^- -pair

is created the Lorentz force caused by the magnetic field, which is parallel to the beam pipe, acts only in azimuthal direction and it will deflect electrons always in the same direction and positrons always in the opposite direction, since they differ in charge. If we define the azimuthal opening angle of the e^+e^- -pair as the azimuthal angle of the electron minus the azimuthal angle of the positron:

$$\Delta\varphi_0 = \varphi_0(e^-) - \varphi_0(e^+) \quad (3.9)$$

we will obtain a parameter which has always the same sign for conversion pairs, because the magnetic field dominates the opening of these pairs compared to their intrinsic opening angle. In contrast, we will get an almost symmetric distribution around zero radians for Dalitz decays. In the case of Dalitz decays the main contribution of the opening angle comes from the π^0 mass. The small asymmetry can be explained by the effect of the magnetic field which still works in the same direction even for Dalitz decays. The distribution of $\Delta\varphi_0$ is shown in Fig. 3.7 for all e^+e^- -pairs (black line), Dalitz decays (red) and conversion pairs (blue) as a result of a Monte Carlo simulations. The $\Delta\varphi_0$ distribution for real data is plotted in Fig. 3.8.

As we can see photon conversions have for the field setting during the $\sqrt{s_{NN}} = 62.4$ GeV run a negative $\Delta\varphi_0$ in the PHENIX coordinate system.

Another consequence of the small opening angle of the photon conversion

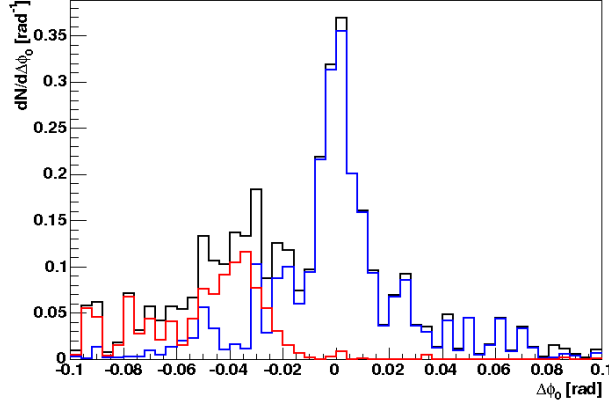


Figure 3.7 The azimuthal opening angle of e^+e^- -pairs from photon conversions (red line) has always a negative sign, where as the Dalitz decays are distributed almost symmetrical around 0. The black line represents all simulated e^+e^- -pairs .

pairs in the beginning is their well defined orientation in the magnetic field. In the moment of creation of the pair – either by a photon conversion or in a Dalitz decay together with a photon – the pair’s opening angle has no preferred direction neither in azimuthal (φ) nor in polar (ϑ) direction. The plane in which the pair splits up is defined by the momentum vectors of the electron and the positron. Thus, we can specify an orientation of this plane with respect to the plane perpendicular to the magnetic field, which is the x-y-plane in the PHENIX coordinate system. We define the angle ψ_{Pair} between these to planes as follows:

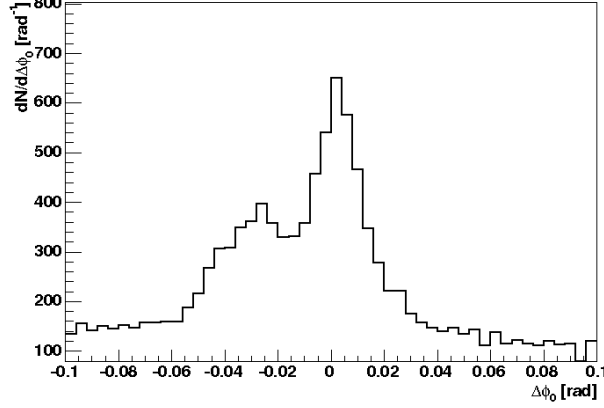


Figure 3.8 The azimuthal opening angle of e^+e^- -pairs in Au + Au collisions at $\sqrt{s_{NN}} = 62.4\text{GeV}$.

$$\Delta\vartheta_0 = \vartheta_0(e^-) - \vartheta_0(e^+) \quad (3.10)$$

$$\xi_{Pair} = \arccos\left(\frac{\vec{p}_{e^-} \cdot \vec{p}_{e^+}}{\|\vec{p}_{e^-}\| \cdot \|\vec{p}_{e^+}\|}\right) \quad (3.11)$$

$$\psi_{Pair} = \arcsin\left(\frac{\Delta\vartheta_0}{\xi_{Pair}}\right) \quad (3.12)$$

So this angle is a measure for the contribution of the opening in polar direction $\Delta\vartheta_0$ to the opening angle ξ_{Pair} . Or in other words what is the contribution of the magnetic field to the orientation of the pair, because it will only influence the opening angle via $\Delta\varphi_0$ but not $\Delta\vartheta_0$. Fig. 3.9 illustrates the orientation of the two planes.

Thus, photon conversions will have a sharp distribution around zero radians in ψ_{Pair} and e^+e^- -pairs from Dalitz decay a rather flat distribution. The

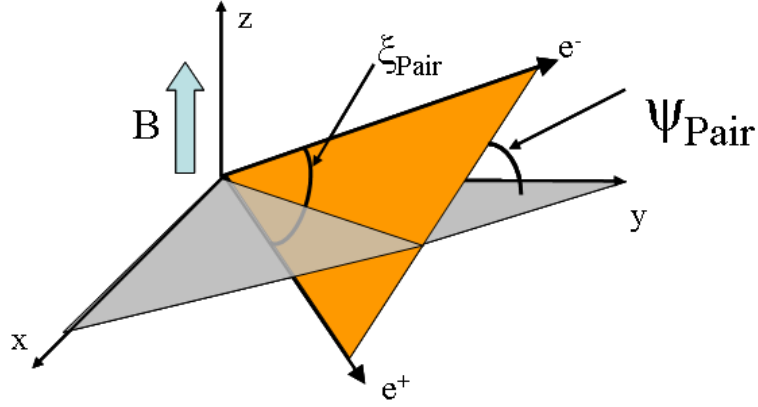


Figure 3.9 Schematic of the pair ordination in the magnetic field. The orange plane is spanned by the momentum vectors of the e^+e^- -pair . The gray shaded plane is the x-y plane which is perpendicular to the magnetic field. The magnetic field is parallel to the beam pipe which is represented by the z axis.

spectrum is shown in Fig. 3.10 as a result of a Monte Carlo simulation and in Fig. 3.11 for real data. These effects lead to a cut on the sign of the azimuthal opening angle ($\Delta\varphi_0 < 0$ rad) and on $|\psi_{Pair}| < 0.2$ rad.

3.4.3 Peak Extraction

Knowing these two parameters, the azimuthal opening angle $\Delta\varphi_0$ and the orientation in the magnetic field ψ_{Pair} , we are now able to extract the beam pipe conversion peak in the invariant mass spectrum, with the following set of cuts:

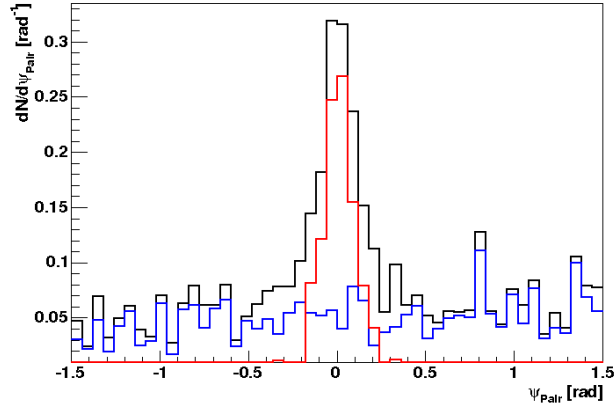


Figure 3.10 The azimuthal opening angle of e^+e^- -pairs from photon conversions (red line) has always a negative sign, whereas the Dalitz decays are distributed almost symmetrical around 0. The black line represents all simulated e^+e^- -pairs .

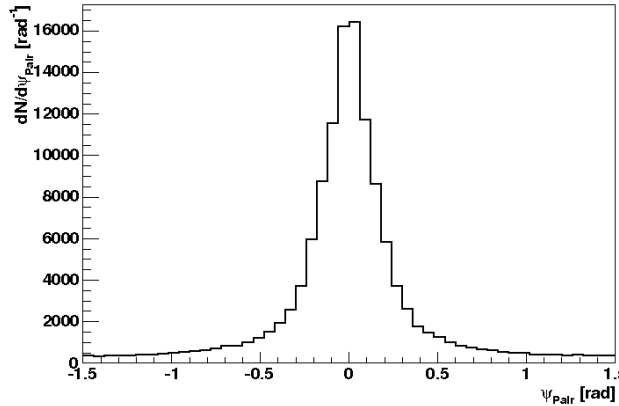


Figure 3.11 ψ_{Pair} is the angle between the plane perpendicular to the magnetic field and the plane which is spanned by the momentum vectors of the e^+e^- -pair in Au + Au collisions at $\sqrt{s_{NN}} = 62.4\text{GeV}$.

- Momentum: $0.150 \text{ GeV}/c \leq p_T \leq 20 \text{ GeV}/c$
- DC track quality: 63 || 51 || 31
- RICH: $n_0 \geq 3 \ \&\& \ n_3 \geq 1 \ \&\& \ \text{disp} \leq 5 \ \&\& \ \chi^2/\text{npe0} \leq 10 \text{ cm}^2$
- Energy-momentum ratio: $0.7 \leq E/p \leq 2.0$
- Matching cuts: $\sqrt{\Delta\varphi_{PC3}^2 + \Delta z_{PC3}^2} \leq 5\sigma \ || \ \sqrt{\Delta\varphi_{EMC}^2 + \Delta z_{EMC}^2} \leq 5\sigma$
- Polar opening angle: $\Delta\varphi_0 < 0 \text{ rad}$
- Pair orientation: $|\psi_{Pair}| < 0.2 \text{ rad}$

The result is shown in 3.12. We can still spot a few e^+e^- -pairs from Dalitz decays at masses below the conversion peak. To get rid of this background ($S/B \approx 1/8$) we use Monte Carlo simulations. Therefore we compare the simulated invariant mass spectrum with the real data in a mass range where we do not expect any conversion pairs ($0 < m_{inv} \leq 0.01 \text{ GeV}/c^2$). We scale the simulated spectrum in this area so the integral underneath matches the real mass spectrum. Afterwards we subtract the scaled Monte Carlo simulations from the real data invariant mass spectrum over the whole range.

With this method we obtain a clean photon conversion peak. You can see the invariant mass peaks for eight p_T bins with a bin width of $200 \text{ MeV}/c$

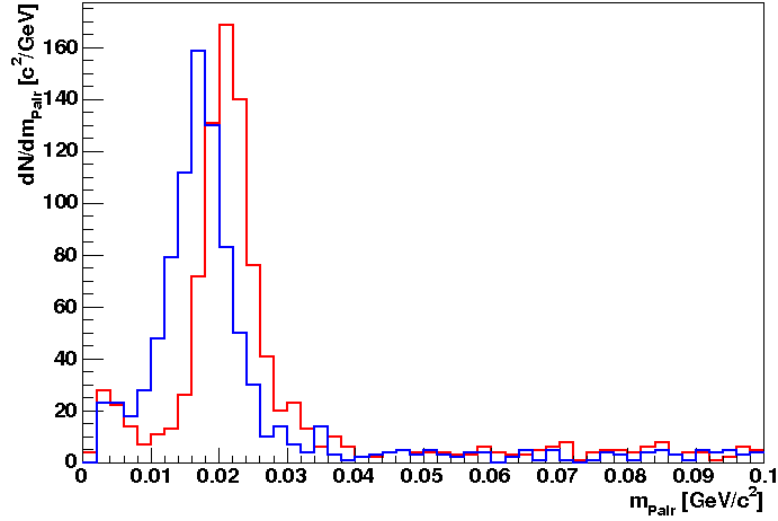


Figure 3.12 Invariant mass spectrum after applying pair cuts. In red you can see pairs in the east arm and in blue pairs in the west arm.

in Fig. 3.13, 3.14 for the east arm and in Fig. 3.15, 3.16 for the west arm, respectively.

$$0.8 < p_T \leq 1.0 \text{ GeV}/c \quad 1.0 < p_T \leq 1.2 \text{ GeV}/c$$

$$1.2 < p_T \leq 1.4 \text{ GeV}/c \quad 1.4 < p_T \leq 1.6 \text{ GeV}/c$$

$$1.6 < p_T \leq 1.8 \text{ GeV}/c \quad 1.8 < p_T \leq 2.0 \text{ GeV}/c$$

$$2.0 < p_T \leq 2.2 \text{ GeV}/c \quad 2.2 < p_T \leq 2.4 \text{ GeV}/c$$

The number of events underneath the conversion peak is summed up to fill a raw photon p_T spectrum shown in Fig. 3.17.

In the next section we are going to calculate the necessary corrections to obtain a final photon p_T spectrum.

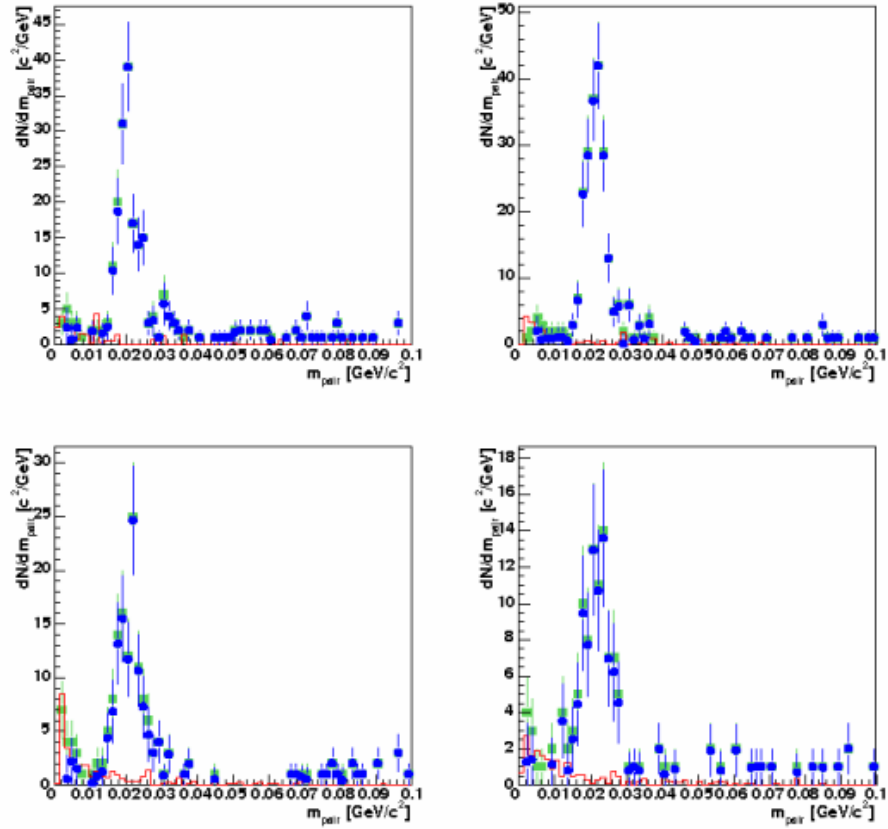


Figure 3.13 Subtracted e^+e^- -pair mass spectrum in the east arm; $0.8 < p_T \leq 1.0$ GeV/c (upper left), $1.0 < p_T \leq 1.2$ GeV/c (upper right), $1.2 < p_T \leq 1.4$ GeV/c (upper left) and $1.4 < p_T \leq 1.6$ GeV/c (lower right). Green: unsubtracted mass spectrum, red: scaled Monte Carlo Dalitz mass distribution, blue: subtracted mass spectrum.

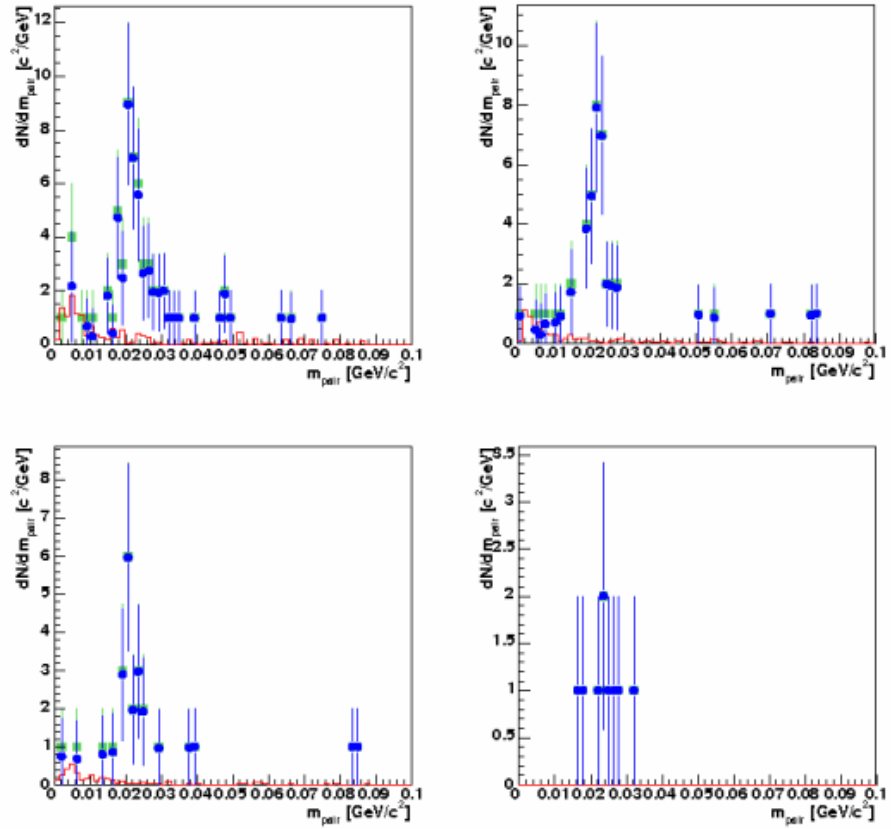


Figure 3.14 Subtracted e^+e^- -pair mass spectrum in the east arm; $1.6 < p_T \leq 1.8$ GeV/c (upper left), $1.8 < p_T \leq 2.0$ GeV/c (upper right), $2.0 < p_T \leq 2.2$ GeV/c (lower left) and $2.2 < p_T \leq 2.4$ GeV/c (lower right). Green: unsubtracted mass spectrum, red: scaled Monte Carlo Dalitz mass distribution, blue: subtracted mass spectrum.

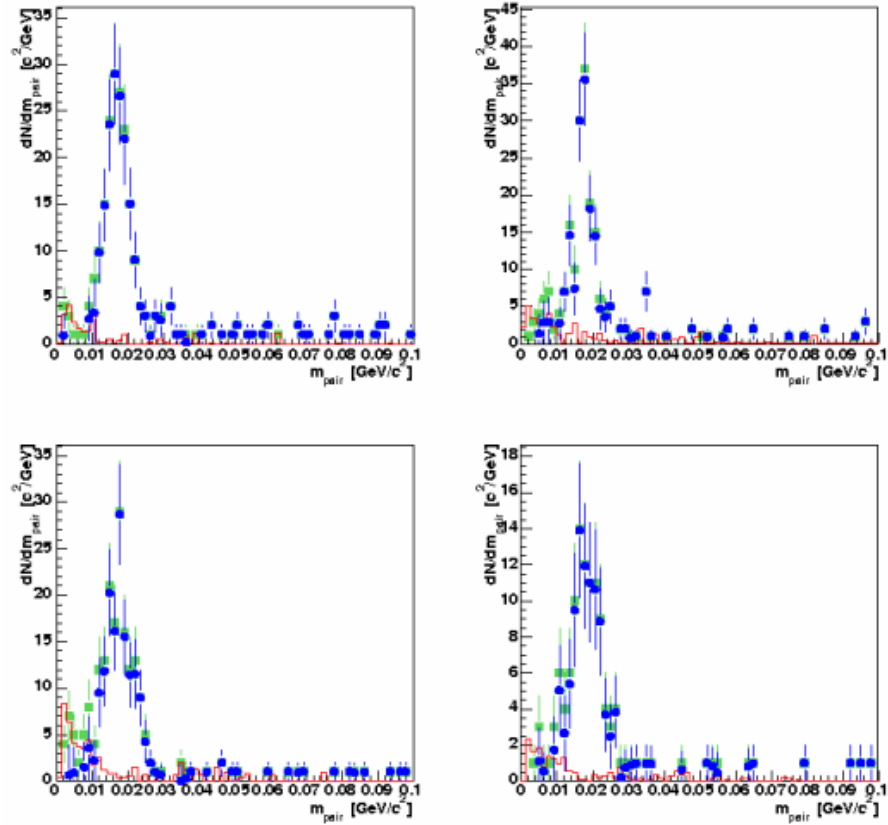


Figure 3.15 Subtracted e^+e^- -pair mass spectrum in the west arm; $0.8 < p_T \leq 1.0$ GeV/c (upper left), $1.0 < p_T \leq 1.2$ GeV/c (upper right), $1.2 < p_T \leq 1.4$ GeV/c (upper left) and $1.4 < p_T \leq 1.6$ GeV/c (lower right). Green: unsubtracted mass spectrum, red: scaled Monte Carlo Dalitz mass distribution, blue: subtracted mass spectrum.

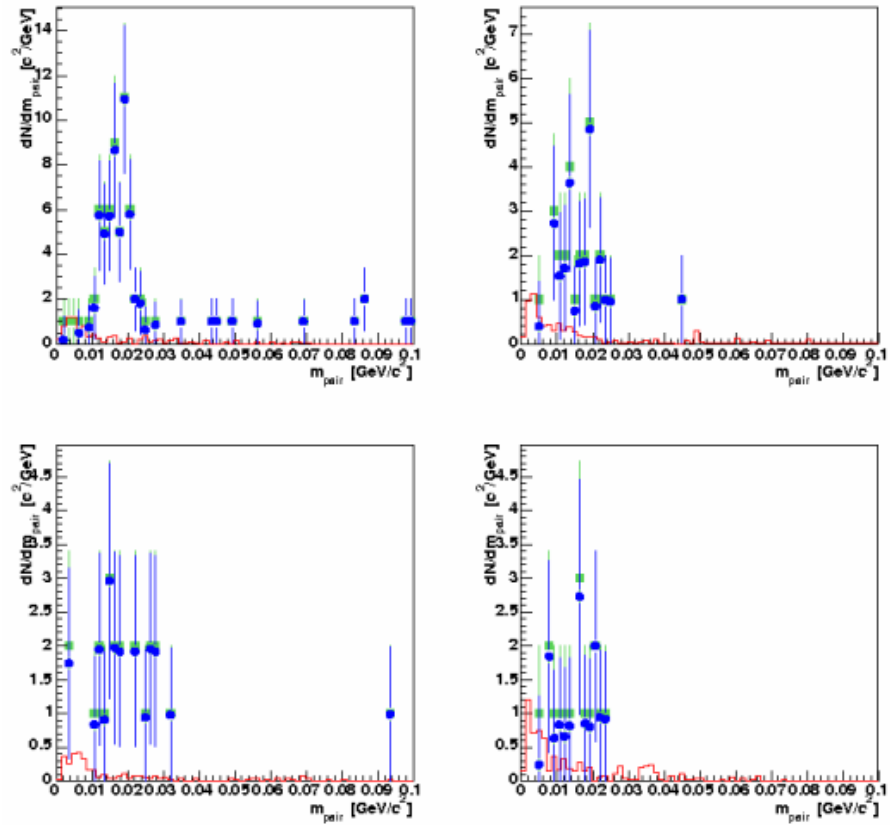


Figure 3.16 Subtracted e^+e^- -pair mass spectrum in the west arm; $1.6 < p_T \leq 1.8$ GeV/c (upper left), $1.8 < p_T \leq 2.0$ GeV/c (upper right), $2.0 < p_T \leq 2.2$ GeV/c (lower left) and $2.2 < p_T \leq 2.4$ GeV/c (lower right). Green: unsubtracted mass spectrum, red: scaled Monte Carlo Dalitz mass distribution, blue: subtracted mass spectrum.

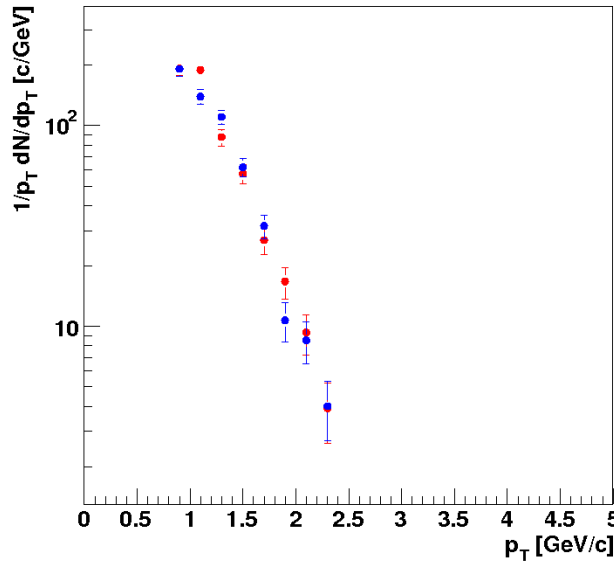


Figure 3.17 Uncorrected photon p_T spectrum in the east arm (red) and the west arm (blue).

3.5 Correction of modified MC Simulation

As mentioned in Chapter 3.3, our correction function will be based on the modified branching ratio so we have to take the change into account. Therefore we plot the e^+e^- -pair p_T spectra of beam pipe conversions for the modified and the unmodified MC simulations for the east arm Fig. 3.18 and for the west arm Fig. 3.19, respectively. Then we calculate the ratio of the integrals underneath the two spectra. For the pairs in the west arm the ratio is: 17.25 and for the east arm: 17.03.

This is what we expect from the change of the average path length to the

next pair production process in Be, as the following calculation shows:

- Unmodified conversion probability:

$$P_{conv} = 1 - \exp(7/9 \cdot x/X_0) \quad \text{with: } x = 0.3 \% \cdot X_0 \quad (3.13)$$

- Modified conversion probability:

$$P_{conv}^* = 1 - \exp(7/9 \cdot x^*/X_0) \quad \text{with: } x^* = 6.0 \% \cdot X_0 \quad (3.14)$$

- Ratio of number of photons from modified and from unmodified conversions (modified π^0 branching ratio is taken into account):

$$f = \frac{(2 \cdot 76.04 \% + 1 \cdot 23.96 \%) \cdot P_{conv}^*}{(2 \cdot 98.802 \% + 1 \cdot 1.198 \%) \cdot P_{conv}} = 17.3$$

Fig. 3.20 and Fig. 3.21 show that the assumption of a p_T independent ratio vs. p_T is legitimate within errors.

3.6 Correction for Acceptance and Efficiency

To correct for acceptance and efficiency losses we used a Monte Carlo simulation of π^0 decays in the PHENIX detector. We compared the input spectrum of photons with the reconstructed e^+e^- -pairs from beam pipe conversion. The ratio is used as a correction function for the raw photon p_T spectrum.

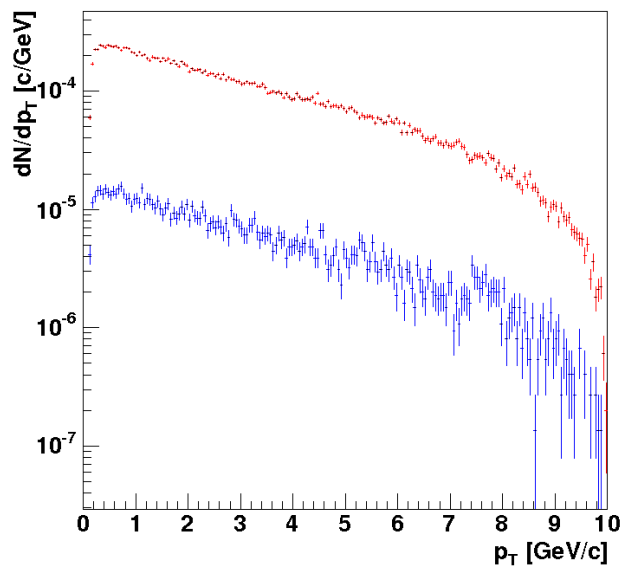


Figure 3.18 Comparison of the modified (red) Monte Carlo p_T spectrum with the unmodified (blue) p_T spectrum in the east arm.

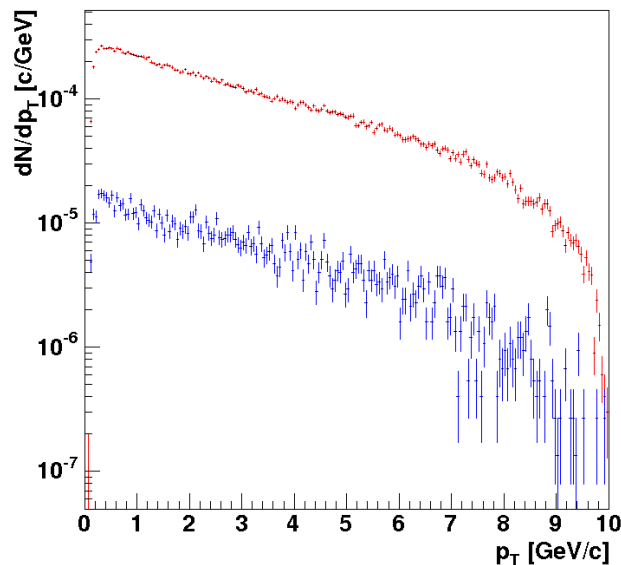


Figure 3.19 Comparison of the modified (red) Monte Carlo p_T spectrum with the unmodified (blue) p_T spectrum in the west arm.

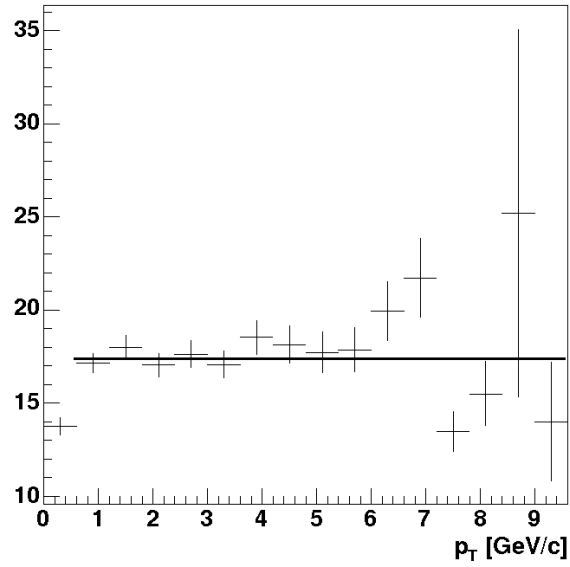


Figure 3.20 Ratio of the modified Monte Carlo p_T spectrum and the unmodified p_T spectrum in the east arm.

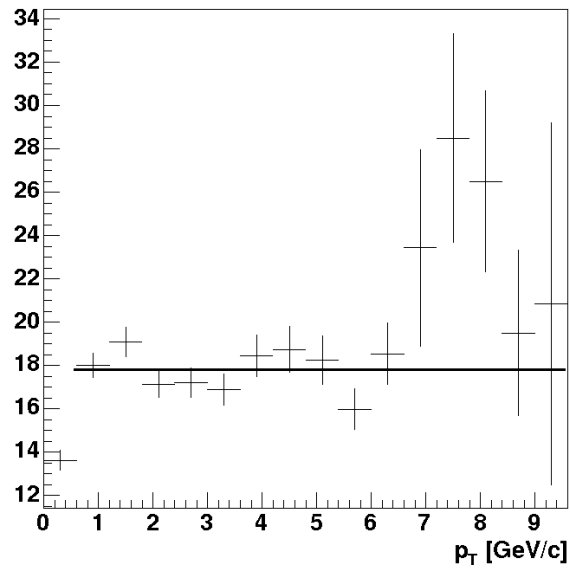


Figure 3.21 Ratio of the modified Monte Carlo p_T spectrum and the unmodified p_T spectrum in the west arm.

In Fig. 3.22 and 3.23 we can see the ratio of the input photon p_T spectrum and the modified output spectrum of beam pipe conversions for the east and the west arm, respectively. The output spectra are obtained by doing all analysis steps which are done for the real data spectra in Fig. 3.17.

To compensate the statistical fluctuation of this ratio we fit the data with a function of the following form:

$$f(p_T) = e^{a-b \cdot p_T} + c \quad (3.15)$$

in a p_T range 0.5–5 GeV/c. The fit result is summarized in Tab 3.6:

Parameter	East Arm	West Arm
a	13.29±0.48	13.17±0.48
b [c/GeV]	1.87±0.32	1.69±0.32
c	2133.46±117.27	2412.53±1524.88

Table 3.3 Fit Parameter of the correction functions for east and west arm

Once we have all the correction factors together we apply these on the spectra in Fig. 3.17. The result is shown in Fig. 3.24.

The lowest point of interest at 0.8 GeV/c is not well represented by the fit (both in east and west arm) we will correct the points at 0.8 GeV/c in the uncorrected photon spectra Fig. 3.17 with the bin value instead of using the fit value.

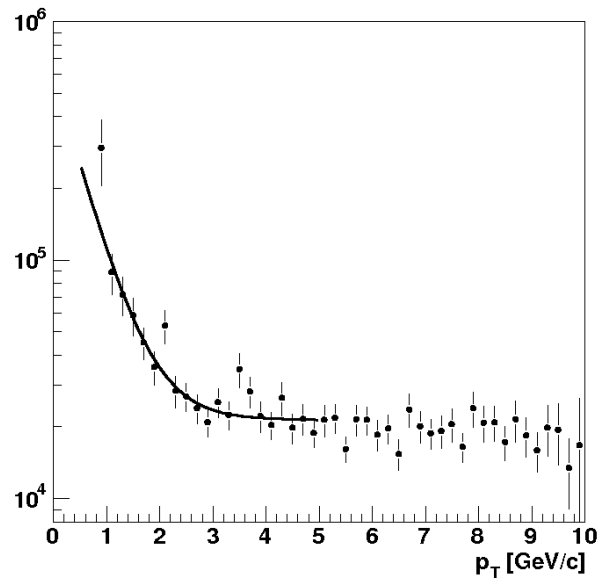


Figure 3.22 Correction function for the detector acceptance and reconstruction efficiency in the east arm.

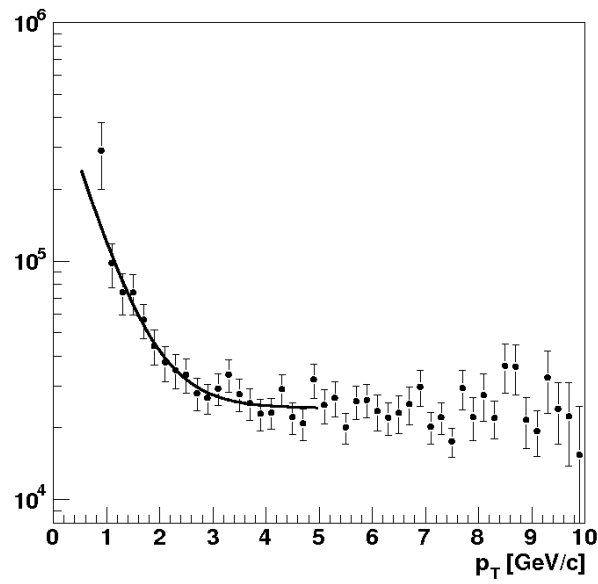


Figure 3.23 Correction function for the detector acceptance and reconstruction efficiency in the west arm.

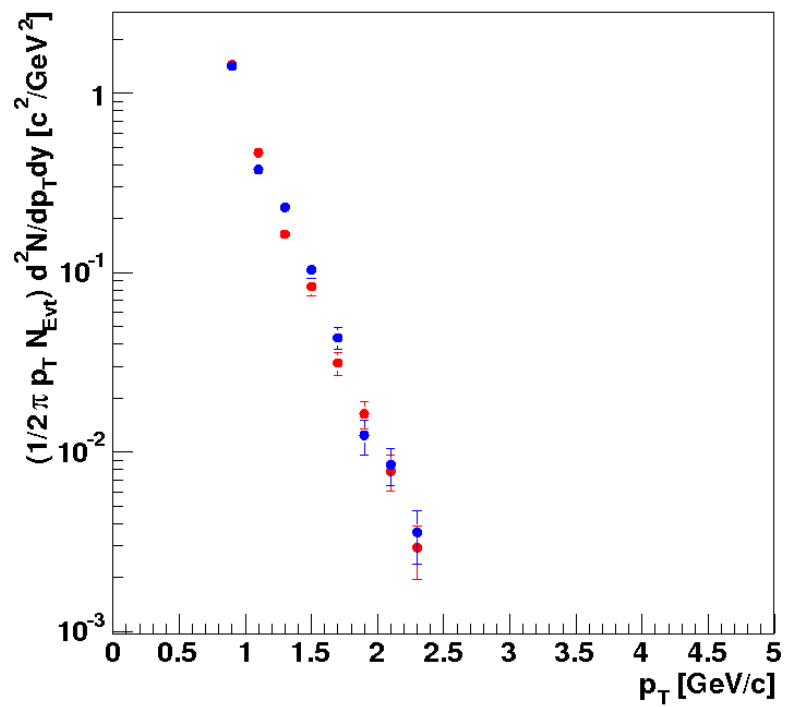


Figure 3.24 Corrected photon p_T spectrum in the east arm (red) and the west arm (blue).

3.7 Cocktail Comparison

In this section we compare our data with a photon p_T spectrum as one would expect from hadronic sources. The EXODUS event generator (see Chapter 3.3) was used to produce such a photon cocktail. It includes the following light meson decays:

- $\pi^0 \rightarrow \gamma\gamma, \pi^0 \rightarrow \gamma e^+ e^-$
- $\eta \rightarrow \gamma\gamma, \eta \rightarrow \gamma e^+ e^-$
- $\omega \rightarrow \gamma\pi^0$
- $\eta' \rightarrow \gamma\gamma, \eta' \rightarrow \gamma e^+ e^-, \eta' \rightarrow \gamma\rho, \eta' \rightarrow \gamma\omega$
- $\phi \rightarrow \gamma\eta$

For the cocktail ingredients EXODUS will use available PHENIX measurements where available. If there is no PHENIX measurement, EXODUS will take the charged and neutral pion spectra and use m_T scaling to simulate the shape of the spectrum. Furthermore it needs the ratio of yields taken at high p_T for a proper normalization. A detailed description of the cocktail can be found in [22],[25] and [26].

Fig. 3.25 – 3.28 show a comparison of the cocktail with the corrected photon p_T spectra.

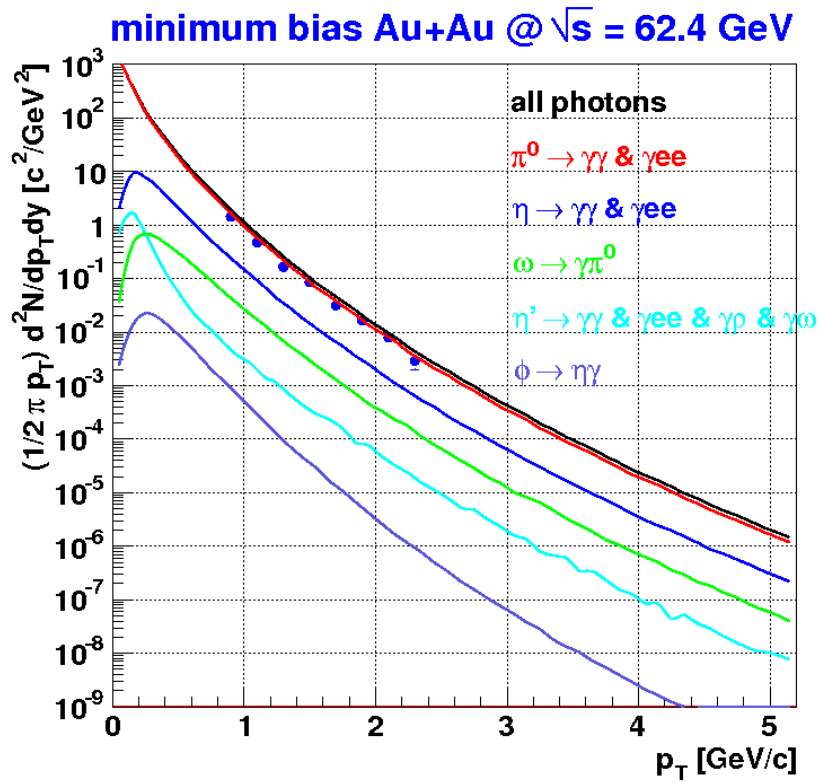


Figure 3.25 Comparison of corrected photon p_T spectrum with cocktail for east arm. Shown are the total photon spectrum (black line) and its components. The photon p_T spectrum of this analysis is plotted in blue points.

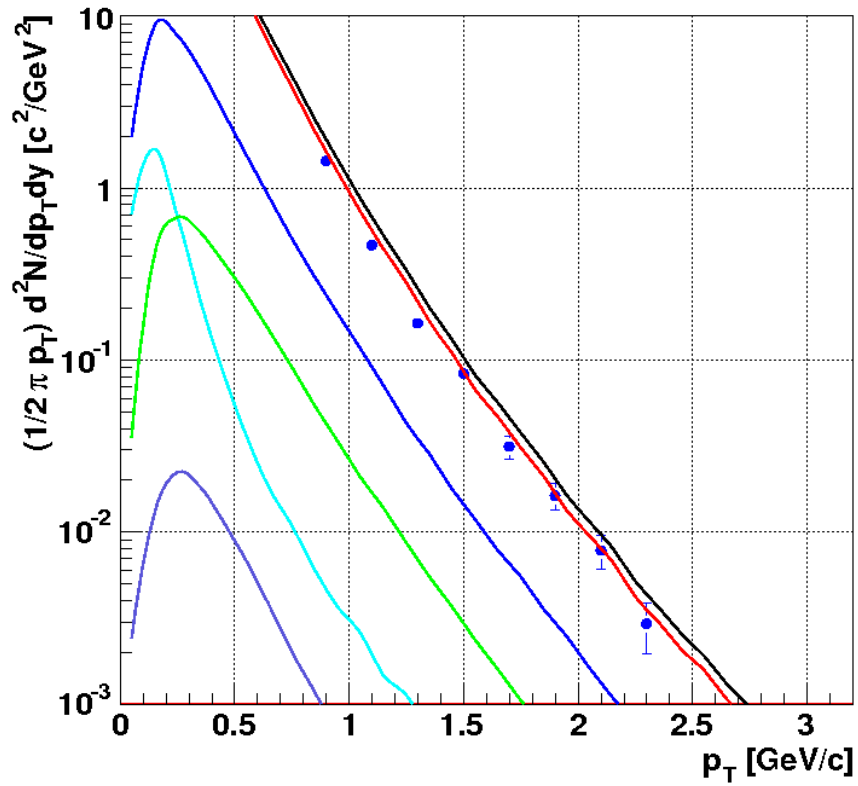


Figure 3.26 Zoom into the comparison of corrected photon p_T spectrum with cocktail for east arm. Shown are the total photon spectrum (black line) and its components. The photon p_T spectrum of this analysis is plotted in blue points.

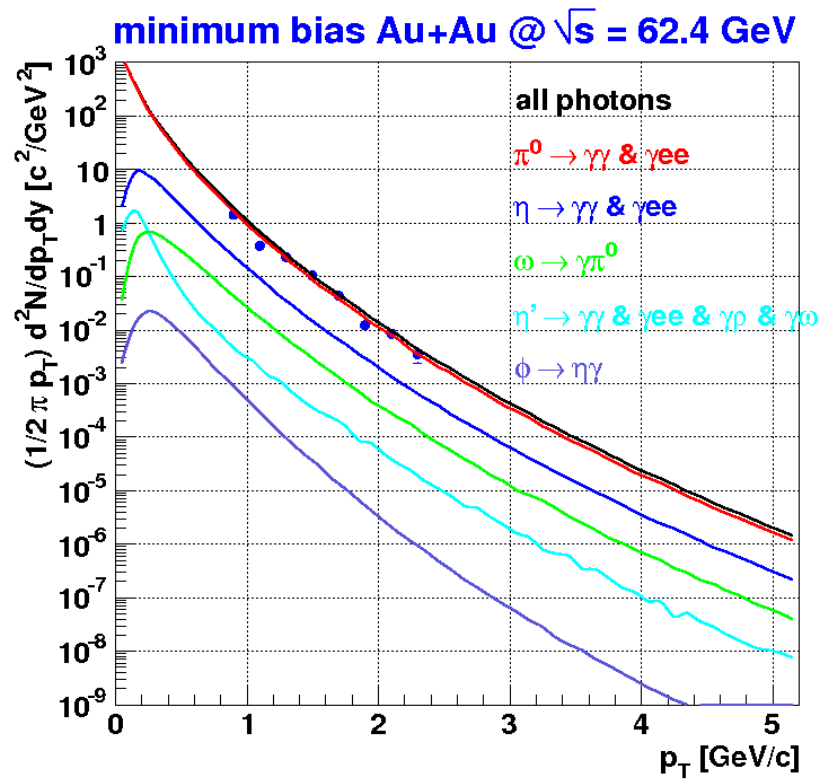


Figure 3.27 Comparison of corrected photon p_T spectrum with cocktail for west arm. Shown are the total photon spectrum (black line) and its components. The photon p_T spectrum of this analysis is plotted in blue points.

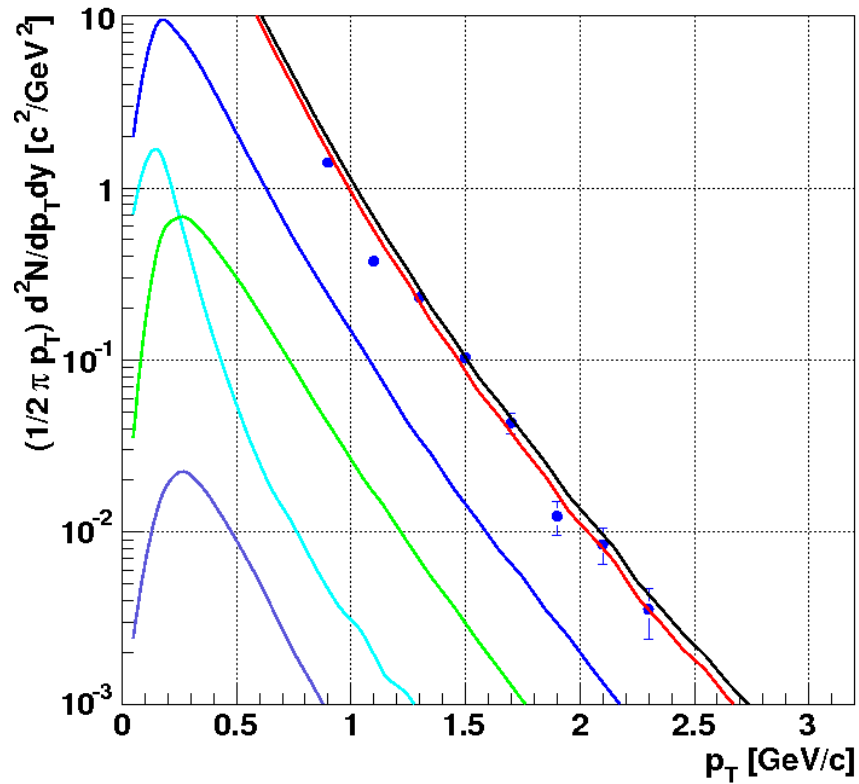


Figure 3.28 Zoom into the comparison of corrected photon p_T spectrum with cocktail for west arm. Shown are the total photon spectrum (black line) and its components. The photon p_T spectrum of this analysis is plotted in blue points.

Chapter 4

Systematic Errors

The following chapter summarizes the systematic errors of this analysis. There are different sources which contribute to the total systematic uncertainty. The choice of electron identification cuts together with cuts to extract beam pipe conversion e^+e^- -pairs are subject of the first section. The cocktail will be discussed afterwards.

4.1 Electron ID and Conversion Cuts

To estimate the systematic error for each electron identification cut we compare for each parameter the fully corrected e^+e^- -pair p_T spectrum of beam pipe conversions for the normal set of cuts with a slightly stronger and a slightly looser cut on the according parameter. Fig. 4.1 – 4.4 show the plots for the associated systematic errors. We obtain the systematic error for a par-

ticular cut by dividing the difference of the p_T bin with the largest difference between the looser and the stronger cut choice by $\sqrt{12}$, since we assume a flat distribution inside each p_T bin.

The systematic uncertainty of the Monte Carlo Simulation is automatically taken into account, because we compare the acceptance and efficiency corrected p_T spectra. If the description of the Monte Carlo Simulation was ideal, all ratios were zero, because the correction function took care of the differences.

Tab. 4.1 lists all systematic errors from electron identification and beam pipe conversion cuts:

Systematic	East Arm	West Arm
n0	7 %	10 %
n3	2 %	1 %
χ^2/n_{pe0}	5%	9 %
displacement	12 %	10 %
e/p	3 %	4 %
pair cuts	12 %	9 %
total	19 %	20 %

Table 4.1 Systematic errors from electron and conversion cuts.

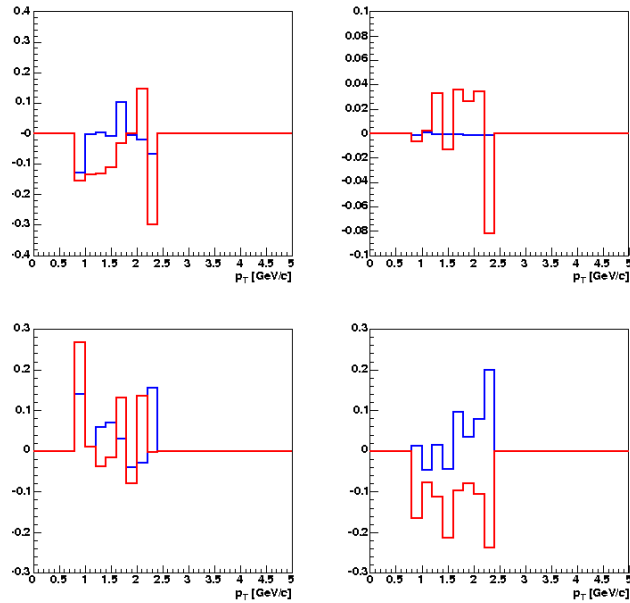


Figure 4.1 Systematic uncertainty of cuts in the east arm. Shown are plots for n_0 (upper left), n_3 (upper right), χ^2/npe_0 (lower left) and $disp$ (lower right).

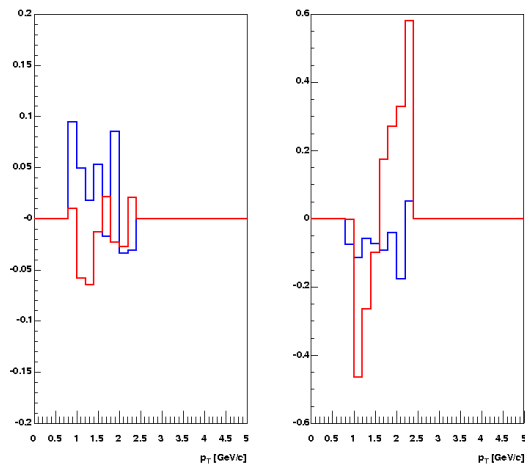


Figure 4.2 Systematic uncertainty of cuts in the east arm. Shown are plots for E/p (left) and conversions (right).

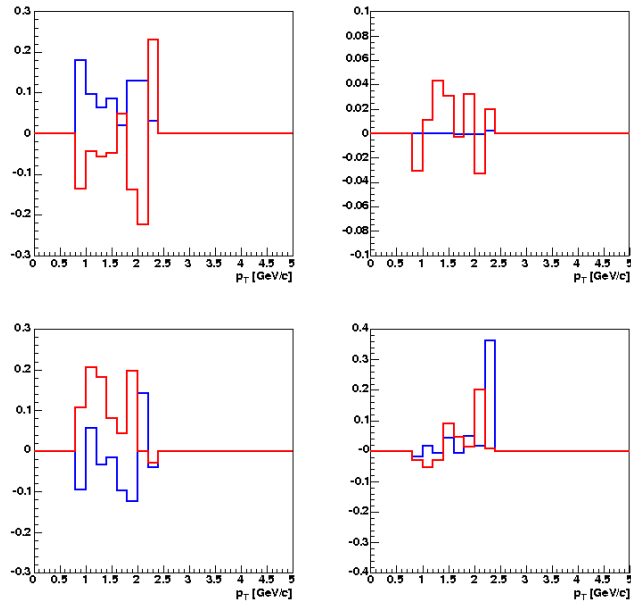


Figure 4.3 Systematic uncertainty of cuts in the west arm. Shown are plots for n_0 (upper left), n_3 (upper right), χ^2/n_{pe0} (lower left) and $disp$ (lower right).

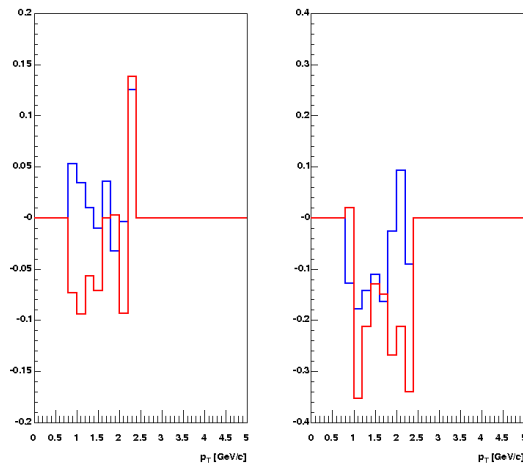


Figure 4.4 Systematic uncertainty of cuts in the west arm. Shown are plots for E/p (left) and conversions (right).

4.2 The Cocktail

For the Cocktail of simulated γ sources in Au + Au collisions at $\sqrt{s_{NN}} = 62.4$ GeV exists only an estimate of the systematic uncertainty. From other cocktails ([22], [25] and [26]) one estimates an overall systematic error of 15 %.

Chapter 5

Result and Summary

In this thesis we presented a new method to measure thermal photons in Au + Au collisions in PHENIX. We showed that we are able to extract photon conversions in the beam pipe from other e^+e^- -pair sources. We achieved a photon spectra in a p_T region 0.8–2.4 GeV/c which agrees with the cocktail within the errors.

In Fig. 5.1 we show the comparison of the photon spectrum (east and west arm combined) in comparison with the cocktail. Furthermore we present a ratio of measured γ and the cocktail in Fig. 5.2.

With the result of this thesis it is not yet possible to see a photon excess in the ratio of measured γ and simulated γ Fig. 5.2. Two major issues are responsible for this:

On the one hand we suffered from the low statistics of the analyzed $\sqrt{s_{NN}} =$

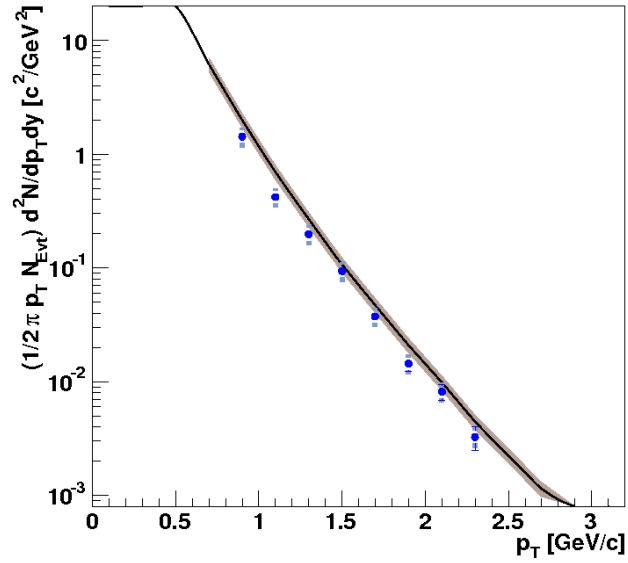


Figure 5.1 Photon p_T spectrum in comparison to the cocktail. Statistical error are shown as error bars; systematic errors as filled rectangles.

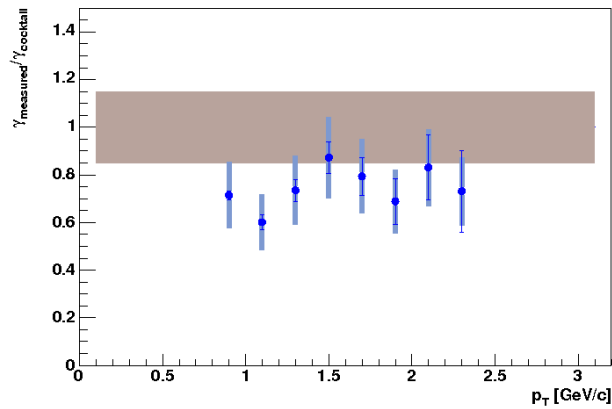


Figure 5.2 Ratio of measured photon p_T spectrum and photons from the cocktail. The systematic error of the cocktail is drawn as error band around 1.

62.4 GeV dataset, since this method is very sensitive to the available statistics; only 0.2 % of all photons convert in the beam pipe material.

On the other hand, the errors in the current analysis is dominated by the systematic uncertainties. The main reason for the high systematic uncertainties is the insufficient understanding of the Monte Carlo simulations. We have to improve the agreement between the simulation and the real data which was not possible within the scope of this thesis.

In the future a better understanding of the simulation should enable us to decrease the systematic errors to a level of ≈ 10 %. Future analysis of the $\sqrt{s_{NN}} = 200$ GeV dataset will also benefit from the statistic which is a multiple of the $\sqrt{s_{NN}} = 62.4$ GeV. Than it may be even possible to obtain photon p_T spectra for different centrality classes.

Bibliography

- [1] D. J. Gross and F. Wilczek, Phys. Rev. Lett. **30**, 1343 (1973).
- [2] D. J. Gross and F. Wilczek, Phys. Rev. D **8**, 3633 (1973).
- [3] H. D. Politzer, Phys. Rev. Lett. **30**, 1346 (1973).
- [4] H. D. Politzer, Phys. Rept. **14**, 129 (1974).
- [5] Cheuk-Yin Wong, “Introduction to High-Energy Heavy-Ion Collisions”,
World Scientific (1994).
- [6] E. V. Shuryak, Phys. Rept. **61**, (1980) 71–158.
- [7] F. Karsch, Lect. Notes Phys. **583**, 209 (2002) [arXiv:hep-lat/0106019].
- [8] K. Adcox *et al.* [PHENIX Collaboration], arXiv:nucl-ex/0410003.
- [9] S. Turbide, R. Rapp and C. Gale, Phys. Rev. C **69**, 014903 (2004)
[arXiv:hep-ph/0308085].

- [10] P. Aurenche, F. Gelis, R. Kobes and H. Zaraket, Phys. Rev. D **58**, 085003 (1998) [arXiv:hep-ph/9804224].
- [11] M. M. Aggarwal *et al.* [WA98 Collaboration], Phys. Rev. Lett. **93**, 022301 (2004) [arXiv:nucl-ex/0310022].
- [12] J. Frantz [PHENIX Collaboration], J. Phys. G **30**, S1003 (2004) [arXiv:nucl-ex/0404006].
- [13] H. Akikawa *et al.*, Nucl. Instrum. Methods Phys. Res., Sect. A **499**, 537 (2003).
- [14] A. J. Baltz, C. Chasman and S. N. White, Nucl. Instrum. Methods Phys. Res., Sect. A **417**, 1 (1998) [arXiv:nucl-ex/9801002].
- [15] C. Adler *et al.*, Nucl. Instrum. Methods Phys. Res., Sect. A **499**, 433 (2003).
- [16] M. Allen *et al.*, Nucl. Instrum. Methods Phys. Res., Sect. A **499**, 549 (2003).
- [17] S. H. Aronson *et al.*, Nucl. Instrum. Methods Phys. Res., Sect. A **499**, 480 (2003).
- [18] K. Adcox *et al.*, Nucl. Instrum. Methods Phys. Res., Sect. A **499**, 489 (2003).

- [19] M. Aizawa *et al.*, Nucl. Instrum. Methods Phys. Res., Sect. A **499**, 508 (2003).
- [20] L. Aphecetche *et al.*, Nucl. Instrum. Methods Phys. Res., Sect. A **499**, 521 (2003).
- [21] T. K. Hemmick, PHENIX internal offline computing mailing list, (2002) URL: <https://www.phenix.bnl.gov/phenix/WWW/p/lists/phenix-off-1/msg07182.html> [as at 2005-10-01].
- [22] R. Aeverbeck *et al.*, PHENIX Analysis Note **89**, (2001).
- [23] Vanderbilt University, PHENIX Simulation Webpage, (2003), URL: <http://vpac17.phy.vanderbilt.edu/simulation/PISA/pisa.html> [as at 2005-10-01].
- [24] L. Aphecetche *et al.*, PHENIX Analysis Note **292**, (2004).
- [25] R. Aeverbeck, PHENIX Analysis Note **253**, (2004).
- [26] R. Aeverbeck, PHENIX Analysis Note **254**, (2004).
- [27] F. Karsch, E. Laermann and A. Peikert, Phys. Lett. B **478**, 447 (2000) [arXiv:hep-lat/0002003].
- [28] M. M. Aggarwal *et al.* [WA98 Collaboration], Phys. Rev. Lett. **85**, 3595 (2000) [arXiv:nucl-ex/0006008].

- [29] J. I. Kapusta, P. Lichard and D. Seibert, Phys. Rev. D **44**, 2774 (1991)
[Erratum-ibid. D **47**, 4171 (1993)].
- [30] E. V. Shuryak, Phys. Lett. B **78**, 150 (1978) [Sov. J. Nucl. Phys. **28**,
408.1978 YAFIA,28,796 (1978 YAFIA,28,796-808.1978)].
- [31] L. D. McLerran and T. Toimela, Phys. Rev. D **31**, 545 (1985).
- [32] J. D. Bjorken, Phys. Rev. D **27**, 140 (1983).
- [33] S. Catani, M. L. Mangano, P. Nason, C. Oleari and W. Vogelsang, JHEP
9903, 025 (1999) [arXiv:hep-ph/9903436].
- [34] S. S. Adler *et al.* [PHENIX Collaboration], Phys. Rev. Lett. **91**, 182301
(2003) [arXiv:nucl-ex/0305013].
- [35] S. S. Adler *et al.* [PHENIX Collaboration], arXiv:nucl-ex/0408007.
- [36] S. S. Adler *et al.* [PHENIX Collaboration], Phys. Rev. C **69**, 034910
(2004) [arXiv:nucl-ex/0308006].
- [37] C. Adler *et al.*, Nucl. Instrum. Methods Phys. Res., Sect. A **470**, 488
(2001).
- [38] K. Adcox *et al.*, Nucl. Instrum. Methods Phys. Res., Sect. A **499**, 469
(2003).

- [39] GEANT - Detector Description and Simulation Tool, URL: <http://wwwasd.web.cern.ch/wwwasd/geant/> [as at 2005-10-01].
- [40] C. F. Maguire, PISA2000 Release Information, (2000) URL: <http://www.phenix.bnl.gov/phenix/WWW/simulation/pisa2000.html> [as at 2005-10-01].
- [41] P. Chand *et al*, A Primer Manual for the PHENIX Simulation Code PISA, (1999), URL: http://www.phenix.bnl.gov/phenix/WWW/simulation/primer4/seq_primer.html [as at 2005-10-01].

Appendix A

Run List

122470, 122472, 122473, 122596, 122597, 122604, 122642, 122644, 122673,
122679, 122680, 122681, 122731, 122735, 122736, 122738, 122740, 122769,
122783, 122784, 122785, 122786, 122846, 122847, 122849, 122850, 122851,
122893, 122894, 122896, 122929, 122931, 122942, 122943, 123037, 123039,
123064, 123068, 123069, 123119, 123120, 123121, 123202, 123203, 123222,
123227, 123235, 123247, 123250, 123335, 123340, 123341, 123347, 123348,
123354, 123356, 123357, 123367, 123369, 123440, 123441, 123442.